SIAM J. IMAGING SCIENCES
Vol. 14, No. 3, pp. 976–1003

Microlocal Analysis of Generalized Radon Transforms from Scattering Tomography*

James W. Webber† and Eric Todd Quinto‡

Abstract. Here we present a novel microlocal analysis of generalized Radon transforms which describe the integrals of L^2 functions of compact support over surfaces of revolution of C^∞ curves q. We show that the Radon transforms are elliptic Fourier integral operators (FIO) and provide an analysis of the left projections Π_L. Our main theorem shows that Π_L satisfies the semiglobal Bolker assumption if and only if $g = q'/q$ is an immersion. An analysis of the visible singularities is presented, after which we derive novel Sobolev smoothness estimates for the generalized Radon FIO. Our theory has specific applications of interest in Emission Compton Scattering Tomography (ECST) and Bragg Scattering Tomography (BST). We show that the ECST and BST integration curves satisfy the semiglobal Bolker assumption and provide simulated reconstructions from ECST and BST data. Additionally, we give example "sinusoidal" integration curves which do not satisfy Bolker and provide simulations of the image artifacts. The observed artifacts in reconstruction are shown to align exactly with our predictions.

Key words. microlocal analysis, scattering tomography, generalized Radon transforms, Sobolev space estimates

AMS subject classifications. 44A12, 45A05

DOI. 10.1137/20M1357305

1. Introduction.

In this paper we present a new microlocal analysis of generalized Radon transforms which describe the integrals of $L^2(\mathbb{R}^n)$ functions of compact support over the surfaces of revolution of $q \in C^\infty((0,\infty))$, which satisfy $\lim_{x_1\to 0^+} q(x_1) = 0$. The surface of revolution of q is generated by rotating the curve defined by q, namely $\{(x_1, 0, \ldots, 0, q(x_1)) : x_1 \in (0,\infty)\}$, about the x_n axis (using $(x_1, x_2, \ldots, x_{n-1}, x_n)$ to represent points in $\mathbb{R}^n$). For example, if $n = 3$ and q defines a straight line through the origin, then the surface of revolution of q would be a cone with central axis x_3 and vertex at the origin. When $n = 2$, the "surface of revolution" is the union of two curves, namely the curve defined by q and its mirror image in the x_2 axis. We denote the union of the reflected curves as "broken-rays" (sometimes denoted by "V-lines" in the literature [5]) when $n = 2$ and the surfaces of revolution as "generalized

*Received by the editors August 3, 2020; accepted for publication (in revised form) April 16, 2021; published electronically July 19, 2021.
https://doi.org/10.1137/20M1357305
Funding: The first author was supported by the U.S. Department of Homeland Security, Science and Technology Directorate, Office of University Programs, under grant 2013-ST-061-ED0001. The work of the second author was partially supported by U.S. National Science Foundation grant DMS 1712207 and Simons Foundation grant 708556. The views and conclusions contained in this document are those of the authors and should not be interpreted as necessarily representing the official policies, either expressed or implied, of the U.S. Department of Homeland Security. Similarly, the opinions, findings, and conclusions or recommendations expressed here do not necessarily reflect the views of the National Science Foundation or the Simons Foundation.

†Department of Oncology and Gynecology, Brigham and Women's Hospital, and Harvard Medical School, Boston, MA 02115 USA (jwebber5@bwh.harvard.edu).
‡Department of Mathematics, Tufts University, Medford, MA 02155 USA (Todd.Quinto@tufts.edu).

cones" when $n \geq 3$. We illustrate the scanning geometry and some example integration curves related to ECST and BST in the $n = 2$ case in Figure 1. The Radon data is n-dimensional and comprised of an $(n-1)$-dimensional translation by $\mathbf{x}_0 \in \mathbb{R}^{n-1}$ and a one-dimensional (1-D) scaling by $E \in (0, \infty)$. We use the notation of [41] in BST, where classically $q = \sin\theta$ denotes the sine of the Bragg angle (θ) and E denotes the photon energy. Also in ECST, E as used here to control the gradient of the red V-lines in Figure 1, is equivalent to the V-line opening angle (or photon scattering angle) and hence to the scattered energy measured at the detector (i.e., E uniquely determines the scattered energy and vice versa) [5]. Hence there is a good practical reason for using E to denote the curve scaling factor. Here we generalize the Radon transforms of [41] and analyze their stability microlocally. Our theory also has applications of interest in gamma ray source imaging in ECST, specifically towards the broken-ray transforms of [1, 2, 5, 10, 11, 12, 28, 37], and the cone Radon transforms of [4, 14, 16, 21, 22, 24, 25, 26, 27, 29, 36, 38, 42].

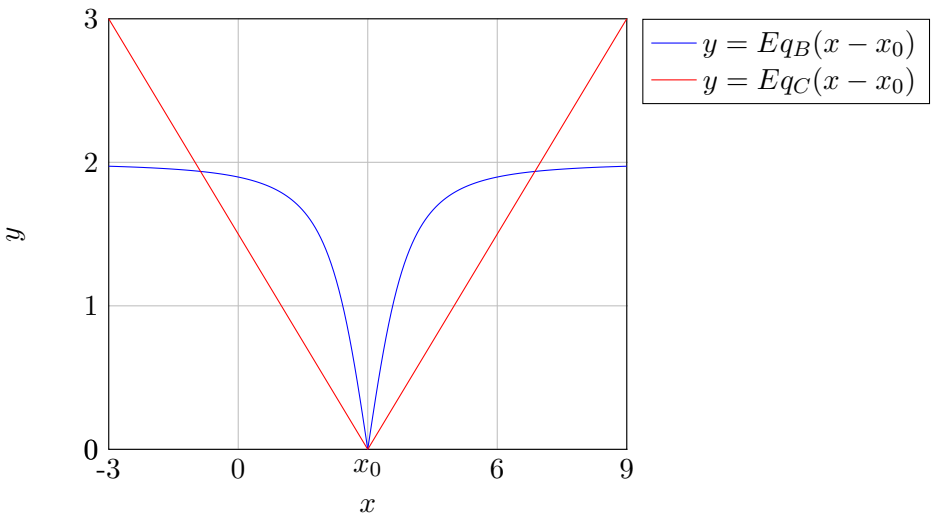

Figure 1. *The scanning geometry. The broken-ray curves displayed are* $q_C(x) = x$ *and* $q_B(x) = \frac{x}{\sqrt{x^2+1}}$, *which are of interest in ECST and BST, respectively. The curves are scaled by* $E > 0$, *translated by* x_0 *along the* x *axis, and reflected in the line* $x = x_0$. *For example, in this case* $x_0 = 3$, $E = 2$ *for* q_B, *and* $E = \frac{1}{2}$ *for* q_C.

The generalized Radon transforms considered here are shown to be elliptic Fourier integral operators (FIOs) of order $\frac{1-n}{2}$, and we give an analysis of the left projections Π_L. Our main theorem proves that Π_L satisfies the semiglobal Bolker assumption (i.e., Π_L is an embedding) if and only if the quotient function $g = q'/q$ is an immersion. Then, we consider the visible singularities in the Radon data and provide Sobolev space estimates for the level of smoothing of the target singularities. This serves to reduce the microlocal and Sobolev analysis of our n-dimensional Radon FIO to the injectivity analysis of the 1-D function g.

We consider two applications of our theory that are of interest, namely Compton camera imaging in ECST and crystalline structure imaging in BST. We show that the ECST and BST integration curves satisfy the conditions of our theorems, which, by implication, proves that the ECST and BST operators are elliptic FIOs which satisfy Bolker. Additionally, we

give example "sinusoidal" q for which the corresponding transforms are shown to violate the semiglobal Bolker assumption. In this case there are artifacts appearing along the q curves at the points where $g = q'/q$ is noninjective. Using the g mapping, we are able to predict precisely the locations of the artifacts in reconstruction. To verify our theory, we present simulated reconstructions of a delta function and a characteristic function on a disc from ECST, BST, and sinusoidal data. The predicted artifacts are shown to align exactly with those observed in reconstruction.

The literature includes the microlocal analysis of broken-ray transforms in [5, 35] and cone Radon transforms in [35, 42]. In [5], the authors analyze the boundary artifacts in reconstruction from broken-ray (denoted V-lines in [5]) integrals, which occur along broken-ray curves at the edge of the data set. A smooth cutoff in the frequency domain is later introduced to combat the boundary artifacts. Proof of FIOs and injectivity analysis of the Π_L is not considered, however. We aim to cover this here for the broken-ray transform. In [42], the author considers the five-dimensional set of cone integrals in $\mathbb{R}^3$, where the cone vertices are constrained to smooth two-dimensional (2-D) surfaces $\mathcal{S}$ in $\mathbb{R}^3$. In [42, Proposition 4] the normal operator of the cone transform is proven to be an elliptic Pseudo Differential Operator (PDO) of order -2 (under certain visibility assumptions), thus implying that the semiglobal Bolker assumption is satisfied. In contrast, for $\mathbb{R}^3$, we consider the three-dimensional subset of the generalized Radon data when the surface of cone vertices $\mathcal{S} = \mathbb{R}^2$ is the (u_1, u_2) plane and the axis of rotation has direction $\beta = (0, 1)$ (using the notation in [42, Example 1]). We prove that the semiglobal Bolker assumption is satisfied here with three-dimensional cone integral data, and our surfaces of integration are more general than cones. In [35, section 4] the n-dimensional case for the cone transform is analyzed microlocally; the generalized Radon integrals are taken over the full set of cones in $\mathbb{R}^n$, and the data set is $2n$-dimensional. In [35, Theorem 14] it is proven that the normal operator of the $2n$-dimensional cone transform is a PDO. We consider the n-dimensional subset of the generalized Radon data where (using the notation of [35]) $\mathbf{u} \in \{u_n = 0\}$ is constrained to the $(u_1, \ldots, u_{n-1})$ plane, and the axis of rotation has direction $\beta = (\mathbf{0}, 1)$. That is, we consider the vertical (i.e., $\beta = (\mathbf{0}, 1)$) cones with vertices on $\{u_n = 0\}$. The results of [35, Theorem 14] are not sufficient to prove Bolker for the n-dimensional set of vertical cone integral data we consider. The vertical cone Radon transform is also considered in [38], but no microlocal analysis is given. We aim to cover this important case here. In addition, our theorems are valid, not only for cones, but for general surfaces of revolution satisfying (3.5).

Our transform is a generalized Radon transform on surfaces of revolution that are generated by translation by directions in the $x_n = 0$ plane. Generalized Radon transforms on surfaces of revolution have been considered in the pure mathematical community, such as [6, 23], but in those articles the surfaces are generated by rotation about the origin not translation in a hyperplane.

In [41] generalized Radon models (denoted by the "Bragg transform") are introduced for crystalline structure imaging in BST and airport baggage screening. The curves of integration in BST are illustrated by q_B in Figure 1. Injectivity proofs and explicit inversion formulae are provided for the Bragg transform in [41, Theorem 4.1]. The stability analysis is not covered, however. We aim to address the stability aspects of the Bragg transform here from a microlocal perspective.

The remainder of this paper is organized as follows. In section 2 we recall some notation and definitions from microlocal analysis which will be used in our theorems. In section 3 we define the generalized cone Radon transform R, which describes the integrals of L^2 functions over the surfaces of revolution of smooth q. We prove that R is an elliptic FIO of order $\frac{1-n}{2}$ and provide expression for the left projection Π_L. We then go on to prove our main theorem, which shows that Π_L is an injective immersion if and only if $g = q'/q$ is an immersion. The smoothing in Sobolev norms is later explained in section 3.4. In section 4 we show that the curves of integration in ECST and BST (as displayed in Figure 1) satisfy the conditions of our theorems, and we provide simulated reconstructions from ECST and BST data. Additionally, in example 4.3, we give example "sinusoidal" q for which g is not an immersion, thus violating Bolker. We provide reconstructions of simulations using these sinusoidal integrals. The observed artifacts are shown to align exactly with our predictions and the theory of section 3.

2. Microlocal definitions. We next provide some notation and definitions. Let X and Y be open subsets of $\mathbb{R}^n$. Let $\mathcal{D}(X)$ be the space of smooth functions compactly supported on X with the standard topology, and let $\mathcal{D}'(X)$ denote its dual space, the vector space of distributions on X. Let $\mathcal{E}(X)$ be the space of all smooth functions on X with the standard topology, and let $\mathcal{E}'(X)$ denote its dual space, the vector space of distributions with compact support contained in X. Finally, let $\mathcal{S}(\mathbb{R}^n)$ be the space of Schwartz functions, which are rapidly decreasing at ∞ along with all derivatives. See [34] for more information.

For a function f in the Schwartz space $\mathcal{S}(\mathbb{R}^n)$ or in $L^2(\mathbb{R}^n)$, we use $\mathcal{F}f$ and $\mathcal{F}^{-1}f$ to denote the Fourier transform and inverse Fourier transform of f, respectively (see [18, Definition 7.1.1]). Note that $\mathcal{F}^{-1}\mathcal{F}f(\mathbf{x}) = \frac{1}{(2\pi)^n}\int_{\mathbf{y}\in\mathbb{R}^n}\int_{\mathbf{z}\in\mathbb{R}^n}\exp((\mathbf{x}-\mathbf{z})\cdot\mathbf{y})\,f(\mathbf{z})\,d\mathbf{z}\,d\mathbf{y}$.

We use the standard multi-index notation: if $\alpha = (\alpha_1, \alpha_2, \dots, \alpha_n) \in \{0, 1, 2, \dots\}^n$ is a multi-index and f is a function on $\mathbb{R}^n$, then

$$\partial^\alpha f = \left(\frac{\partial}{\partial x_1}\right)^{\alpha_1}\left(\frac{\partial}{\partial x_2}\right)^{\alpha_2}\cdots\left(\frac{\partial}{\partial x_n}\right)^{\alpha_n} f.$$

If f is a function of $(\mathbf{y}, \mathbf{x}, \mathbf{s})$, then $\partial^\alpha_{\mathbf{y}} f$ and $\partial^\alpha_{\mathbf{s}} f$ are defined similarly.

We identify cotangent spaces on Euclidean spaces with the underlying Euclidean spaces, so we identify $T^*(X)$ with $X \times \mathbb{R}^n$.

If ϕ is a function of $(\mathbf{y}, \mathbf{x}, \mathbf{s}) \in Y \times X \times \mathbb{R}^N$, then we define $d_{\mathbf{y}}\phi = \left(\frac{\partial\phi}{\partial y_1}, \frac{\partial\phi}{\partial y_2}, \dots, \frac{\partial\phi}{\partial y_n}\right)$, and $d_{\mathbf{x}}\phi$ and $d_{\mathbf{s}}\phi$ are defined similarly. We let $d\phi = \left(d_{\mathbf{y}}\phi, d_{\mathbf{x}}\phi, d_{\mathbf{s}}\phi\right)$.

We use the convenient notation that if $A \subset \mathbb{R}^m$, then $\dot{A} = A \setminus \mathbf{0}$.

The singularities of a function and the directions in which they occur are described by the wavefront set [8, page 16].

Definition 2.1. *Let X be an open subset of $\mathbb{R}^n$, and let f be a distribution in $\mathcal{D}'(X)$. Let $(\mathbf{x}_0, \boldsymbol{\xi}_0) \in X \times \dot{\mathbb{R}}^n$. Then f is* smooth at $\mathbf{x}_0$ in direction $\boldsymbol{\xi}_0$ *if there exists a neighborhood U of $\mathbf{x}_0$ and V of $\boldsymbol{\xi}_0$ such that for every $\phi \in \mathcal{D}(U)$ and $N \in \mathbb{R}$ there exists a constant C_N such that for all $\boldsymbol{\xi} \in V$,*

$$|\mathcal{F}(\phi f)(\lambda\boldsymbol{\xi})| \le C_N(1 + |\lambda|)^{-N}. \tag{2.1}$$

The pair $(\mathbf{x}_0, \boldsymbol{\xi}_0)$ is in the wavefront set, $\mathrm{WF}(f)$, *if f is not smooth at $\mathbf{x}_0$ in direction $\boldsymbol{\xi}_0$.*

This definition follows the intuitive idea that the elements of $\mathrm{WF}(f)$ are the point-normal vector pairs above points of X at which f has singularities. For example, if f is the characteristic function of the unit ball in $\mathbb{R}^3$, then its wavefront set is $\mathrm{WF}(f) = \{(\mathbf{x}, t\mathbf{x}) : \mathbf{x} \in S^2, t \neq 0\}$, the set of points on a sphere paired with the corresponding normal vectors to the sphere.

The wavefront set of a distribution on X is normally defined as a subset of the cotangent bundle $T^*(X)$ so it is invariant under diffeomorphisms, but we do not need this invariance, so we will continue to identify $T^*(X) = X \times \mathbb{R}^n$ and consider $\mathrm{WF}(f)$ as a subset of $X \times \dot{\mathbb{R}}^n$.

Definition 2.2 (see [18, Definition 7.8.1]). *We define $S^m(Y \times X \times \mathbb{R}^N)$ to be the set of $a \in \mathcal{E}(Y \times X \times \mathbb{R}^N)$ such that for every compact set $K \subset Y \times X$ and all multi-indices α, β, γ the bound*

$$\left|\partial_{\mathbf{y}}^{\gamma}\partial_{\mathbf{x}}^{\beta}\partial_{\boldsymbol{\sigma}}^{\alpha} a(\mathbf{y}, \mathbf{x}, \boldsymbol{\sigma})\right| \leq C_{K,\alpha,\beta,\gamma}(1 + \|\boldsymbol{\sigma}\|)^{m-|\alpha|}, \quad (\mathbf{y}, \mathbf{x}) \in K, \ \boldsymbol{\sigma} \in \mathbb{R}^N,$$

holds for some constant $C_{K,\alpha,\beta,\gamma} > 0$.

The elements of S^m are called symbols *of order m. Note that these symbols are sometimes denoted $S^m_{1,0}$. The symbol $a \in S^m(Y, X, \mathbb{R}^N)$ is* elliptic *if for each compact set $K \subset Y \times X$, there is a $C_K > 0$ and $M > 0$ such that*

$$|a(\mathbf{y}, \mathbf{x}, \boldsymbol{\sigma})| \geq C_K(1 + \|\boldsymbol{\sigma}\|)^m, \quad (\mathbf{y}, \mathbf{x}) \in K, \ \|\boldsymbol{\sigma}\| \geq M. \tag{2.2}$$

Definition 2.3 (see [19, Definition 21.2.15]). *A function $\phi = \phi(\mathbf{y}, \mathbf{x}, \boldsymbol{\sigma}) \in \mathcal{E}(Y \times X \times \dot{\mathbb{R}}^N)$ is a* phase function *if $\phi(\mathbf{y}, \mathbf{x}, \lambda\boldsymbol{\sigma}) = \lambda\phi(\mathbf{y}, \mathbf{x}, \boldsymbol{\sigma})$ $\forall \lambda > 0$ and $\mathrm{d}\phi$ is nowhere zero. The* critical set *of ϕ is*

$$\Sigma_\phi = \{(\mathbf{y}, \mathbf{x}, \boldsymbol{\sigma}) \in Y \times X \times \dot{\mathbb{R}}^N : \mathrm{d}_{\boldsymbol{\sigma}}\phi = 0\}.$$

A phase function is clean *if the critical set $\Sigma_\phi = \{(\mathbf{y}, \mathbf{x}, \boldsymbol{\sigma}) : \mathrm{d}_{\boldsymbol{\sigma}}\phi(\mathbf{y}, \mathbf{x}, \boldsymbol{\sigma}) = 0\}$ is a smooth manifold with tangent space defined as the kernel of $d\,(d_\sigma\phi)$ on Σ_ϕ. Here, the derivative d is applied componentwise to the vector-valued function $d_\sigma\phi$. So, $d\,(d_\sigma\phi)$ is treated as a Jacobian matrix of dimensions $N \times (2n + N)$.*

By the constant rank theorem the requirement for a phase function to be clean is satisfied if $\mathrm{d}\big(\mathrm{d}_{\boldsymbol{\sigma}}\phi\big)$ has constant rank.

Definition 2.4 (see [19, Definition 21.2.15] and [20, section 25.2]). *Let X and Y be open subsets of $\mathbb{R}^n$. Let $\phi \in \mathcal{E}\big(Y \times X \times \dot{\mathbb{R}}^N\big)$ be a clean phase function. In addition, we assume that ϕ is* nondegenerate *in the following sense:*

$$\mathrm{d}_{\mathbf{y}}\phi \text{ and } \mathrm{d}_{\mathbf{x}}\phi \text{ are never zero on } \Sigma_\phi.$$

The canonical relation *parametrized by ϕ is defined as*

$$\mathcal{C} = \left\{\left(\left(\mathbf{y}, \mathrm{d}_{\mathbf{y}}\phi(\mathbf{y}, \mathbf{x}, \boldsymbol{\sigma})\right); \left(\mathbf{x}, -\mathrm{d}_{\mathbf{x}}\phi(\mathbf{y}, \mathbf{x}, \boldsymbol{\sigma})\right)\right) : (\mathbf{y}, \mathbf{x}, \boldsymbol{\sigma}) \in \Sigma_\phi\right\}. \tag{2.3}$$

Definition 2.5. *Let X and Y be open subsets of $\mathbb{R}^n$. Let an operator $A : \mathcal{D}(X) \to \mathcal{D}'(Y)$ be defined by the distribution kernel $K_A \in \mathcal{D}'(X \times Y)$, in the sense that $Af(\mathbf{y}) = \int_X K_A(\mathbf{x}, \mathbf{y}) f(\mathbf{x})\, \mathrm{d}\mathbf{x}$. Then we call K_A the* Schwartz kernel *of A. A* Fourier integral operator (FIO) *of order*

$m+N/2-n/2$ is an operator $A:\mathcal{D}(X)\to\mathcal{D}'(Y)$ with Schwartz kernel given by an oscillatory integral of the form

$$K_A(\mathbf{y},\mathbf{x})=\int_{\mathbb{R}^N} e^{i\phi(\mathbf{y},\mathbf{x},\boldsymbol{\sigma})}a(\mathbf{y},\mathbf{x},\boldsymbol{\sigma})\mathrm{d}\boldsymbol{\sigma}, \tag{2.4}$$

where ϕ is a clean nondegenerate phase function and a is a symbol in $S^m(Y\times X\times\mathbb{R}^N)$. The canonical relation of A *is the canonical relation of ϕ defined in* (2.3).

The FIO A is elliptic *if its symbol is elliptic.*

This is a simplified version of the definition of a FIO in [7, section 2.4] or [20, section 25.2] that is suitable for our purposes since our phase functions are global. Because we assume phase functions are nondegenerate, our FIO can be extended as maps from $\mathcal{D}(X)$ to $\mathcal{E}(Y)$ to maps from $\mathcal{E}'(X)$ to $\mathcal{D}'(Y)$, and sometimes larger sets. For general information about FIOs, see [7, 20, 19]. For information about the Schwartz Kernel, see [18, Theorem 5.1.9].

Let X and Y be sets, and let $\Omega_1\subset X$ and $\Omega_2\subset Y\times X$. The composition $\Omega_2\circ\Omega_1$ and transpose Ω_2^t of Ω_2 are defined as

$$\Omega_2\circ\Omega_1=\{,\}\, y\in Y:\exists x\in\Omega_1,\ (y,x)\in\Omega_2,$$
$$\Omega_2^t=\{(x,y):(y,x)\in\Omega_2\}.$$

The Hörmander–Sato lemma provides the relationship between the wavefront set of distributions and their images under FIOs.

Theorem 2.6 (see [18, Theorem 8.2.13]). *Let $f\in\mathcal{E}'(X)$, and let $A:\mathcal{E}'(X)\to\mathcal{D}'(Y)$ be an FIO with canonical relation $\mathcal{C}$. Then,* $\mathrm{WF}(Af)\subset\mathcal{C}\circ\mathrm{WF}(f)$.

Definition 2.7. *Let $\mathcal{C}\subset T^*(Y\times X)$ be the canonical relation associated to the FIO $A:\mathcal{E}'(X)\to\mathcal{D}'(Y)$. We let Π_L and Π_R denote the natural left- and right-projections of $\mathcal{C}$, projecting onto the appropriate coordinates: $\Pi_L:\mathcal{C}\to T^*(Y)$ and $\Pi_R:\mathcal{C}\to T^*(X)$.*

Because ϕ is nondegenerate, the projections do not map to the zero section.

Let A be an FIO with adjoint A^*. If A satisfies our next definition, then A^*A (or, if A does not map to $\mathcal{E}'(Y)$, then $A^*\psi A$ for an appropriate cutoff ψ) is a PDO [15, 32].

Definition 2.8. *Let $A:\mathcal{E}'(X)\to\mathcal{D}'(Y)$ be an FIO with canonical relation $\mathcal{C}$; then A (or $\mathcal{C}$) satisfies the* semiglobal Bolker assumption *if the natural projection $\Pi_L:\mathcal{C}\to T^*(Y)$ is an embedding (injective immersion).*

3. The main theorem.

In this section we define our transform and give conditions under which our transform satisfies the semiglobal Bolker assumption. We consider a Radon transform in $\mathbb{R}^n$ that is a generalization of the transforms studied in [5, 36, 41, 42]. This transform will integrate on surfaces of revolution with vertex on the $x_n=0$ hyperplane.

We start with the function that will define the surfaces.

$$\begin{gathered}\text{Let } q:[0,\infty)\to[0,\infty) \text{ be continuous on } [0,\infty),\ C^\infty \text{ on } (0,\infty),\\ q(0)=0, \text{ and } q(r)>0 \text{ if } r>0.\end{gathered} \tag{3.1}$$

If $\mathbf{x}=(x_1,x_2,\dots,x_n)\in\mathbb{R}^n$, then we let $\mathbf{x}'=(x_1,x_2,\dots,x_{n-1})\in\mathbb{R}^{n-1}$ so $\mathbf{x}=(\mathbf{x}',x_n)$. Now, let $X=\{(\mathbf{x}',x_n):\mathbf{x}'\in\mathbb{R}^{n-1},x_n\in(0,\infty)\}$ denote the half-space $x_n>0$ in $\mathbb{R}^n$. Let

$Y = (0,\infty)\times\mathbb{R}^{n-1}$. Then, for $(E,\mathbf{x}_0)\in Y$, the surface of integration of our generalized Radon transform is given by

$$S(E,\mathbf{x}_0) = \left\{(\mathbf{x}',x_n)\in X : x_n = Eq\big(\|\mathbf{x}'-\mathbf{x}_0\|\big)\ \mathbf{x}'\in\mathbb{R}^{n-1}\setminus\{\mathbf{x}_0\}\right\}. \tag{3.2}$$

Note that $S(E,\mathbf{x}_0)$ has axis of rotation $\{(\mathbf{x}_0,x_n) : x_n>0\}$ and vertex at $(\mathbf{x}_0,0)$ (which is not in $S(E,\mathbf{x}_0)$). The surface $S(E,\mathbf{x}_0)$ is characterized by the equation

$$\begin{gathered}\Psi(E,\mathbf{x}_0,(\mathbf{x}',x_n)) = 0, \quad \text{where}\\ \Psi(E,\mathbf{x}_0,(\mathbf{x}',x_n)) := x_n - Eq\big(\|\mathbf{x}'-\mathbf{x}_0\|\big).\end{gathered} \tag{3.3}$$

The *generalized cone Radon transform* is given, for $f\in L^2_c(X)$, by

$$\begin{aligned}Rf(E,\mathbf{x}_0) &= \int_{\mathbf{x}\in S(E,\mathbf{x}_0)} f(\mathbf{x})\mathrm{d}S(\mathbf{x})\\ &= \int_{(\mathbf{x},x_n)\in X} f(\mathbf{x}',x_n)\,\|\nabla_{\mathbf{x}}\Psi\|\,\delta\big(\Psi(E,\mathbf{x}_0,(\mathbf{x}',x_n))\big)\mathrm{d}\mathbf{x}'\,\mathrm{d}x_n,\end{aligned} \tag{3.4}$$

where we use [30, eq. (1)] and the relation of the transform M_Ψ in that article to R (see also [18, section 6.1]). Thus, $Rf(E,\mathbf{x}_0)$ integrates f over the surface of revolution $S(E,\mathbf{x}_0)$ with respect to the surface area measure $\mathrm{d}S$. Because R is a Radon transform on smooth manifolds that smoothly foliate X, R is defined on domain $f\in L^2_c(\mathbb{R}^n)$ although Rf is defined only pointwise almost everywhere.

Our first main theorem allows us to analyze mapping properties of R microlocally and in Sobolev space.

Theorem 3.1. *Let $q:[0,\infty)\to[0,\infty)$ satisfy (3.1). Then, the associated generalized cone Radon transform R is an elliptic FIO of order $\frac{1-n}{2}$.*

Let $g = q'/q$ and assume $g:(0,\infty)\to(0,\infty)$. Then, the transform R satisfies the semiglobal Bolker assumption if and only if

$$g'(r)\neq 0 \text{ for all } r\in(0,\infty). \tag{3.5}$$

This condition is equivalent to $qq''-(q')^2$ being nowhere zero for $r\in(0,\infty)$.

Remark 3.2. First, note that Theorem 3.1 is valid for all generalized Radon transforms defined on surfaces $S(E,\mathbf{x}_0)$ for which q and g satisfy the conditions in Theorem 3.1 and the weights on the surfaces are smooth and nowhere zero. That is, for general, smooth, nonvanishing weights on the surfaces of integration, Theorem 3.1 holds. This is true because our proofs present an analysis of the phase function of the generalized Radon FIO, which does not depend on the specific smooth weight. For example, in ECST and BST, we could model the effects due to the attenuation of the incoming and scattered rays as an additional smooth, nonvanishing weight to the surface integrals, under the assumption that the attenuation map can be modeled as smooth. We do not consider such practical concerns in this paper, but it may be of interest to some readers to know how our microlocal theory applies when smoothly attenuative effects are considered in the modeling. In regards to ellipticity, the ellipticity of

R follows because the smooth weight is assumed to be nowhere zero, and thus the conditions of Definition 2.2 are satisfied.

Let $\mathcal{C}$ be the canonical relation of R. For the semiglobal Bolker assumption to hold, $\Pi_L : \mathcal{C} \to T^*(Y)$ needs to be both injective and immersive. In our proof, we will show that (3.5) is equivalent to Π_L being immersive. We will also show that the condition

$$g : (0, \infty) \to (0, \infty) \text{ is injective} \tag{3.6}$$

and is equivalent to Π_L being injective. However, condition (3.5) implies this new condition (3.6) for the following reason: if g' is never 0, then g must be strictly monotonic because the domain of g, $(0, \infty)$, is connected.

3.1. Start of the proof of Theorem 3.1. We do the proof in steps. In this section, we show R is an elliptic FIO and we calculate the canonical relation of R, in general. Then we show that R satisfies the semiglobal Bolker assumption, for $n = 2$ in section 3.2 and, in general, in section 3.3.

The function $\Psi(E, \mathbf{x}_0, \mathbf{x}) = x_n - Eq(\|\mathbf{x}' - \mathbf{x}_0\|)$ is not smooth when $\mathbf{x}' = \mathbf{x}_0$ because of the norm in its definition. We will now smooth out Ψ in a way that does not change Ψ in a neighborhood of the set $\Psi(E, \mathbf{x}_0, \mathbf{x}) = 0$ that defines the Radon transform R. This will allow us to define R in (3.4) using a weight that is smooth on $Y \times X$. We will use this to show that R is a standard FIO with smooth symbol and phase.

Lemma 3.3. *There is a smooth function $\widetilde{\Psi} : Y \times X \to \mathbb{R}$ that is equal to Ψ on an open neighborhood V of*

$$\mathcal{S} = \{(E, \mathbf{x}_0, \mathbf{x}) \in Y \times X : \mathbf{x} \in S(E, \mathbf{x}_0)\} \tag{3.7}$$

in $Y \times X$. For $(E, \mathbf{x}_0, \mathbf{x}) \in Y \times X$, $\widetilde{\Psi}(E, \mathbf{x}_0, \mathbf{x}) = 0$ if and only if $\Psi(E, \mathbf{x}_0, \mathbf{x}) = 0$.

The proof is fairly technical and is given in Appendix A. Note that $\widetilde{\Psi}$ will have a singularity at points with $x_n = 0$, but those points are not in X and the functions we evaluate R on are supported away from $x_n = 0$.

Corollary 3.4. *Let $\widetilde{\Psi}$ be the function given in Lemma 3.3; then the generalized Radon transform R defined in (3.4) is an elliptic FIO of order $(1 - n)/2$ given by*

$$Rf(E, \mathbf{x}_0) = \int_{\mathbb{R}^n} \int_{\mathbb{R}} \exp\left(\widetilde{\Phi}(E, \mathbf{x}_0, \mathbf{x})\right) a(E, \mathbf{x}_0, \mathbf{x}) \, \mathrm{d}\sigma \mathrm{d}\mathbf{x}, \tag{3.8}$$

where

$$\widetilde{\Phi}(E, \mathbf{x}_0, \mathbf{x}) = \sigma \widetilde{\Psi}(E, \mathbf{x}_0, \mathbf{x}), \tag{3.9}$$

$$a(E, \mathbf{x}_0, \mathbf{x}) = \left\|\nabla_{\mathbf{x}} \widetilde{\Psi}(E, \mathbf{x}_0, \mathbf{x})\right\|. \tag{3.10}$$

The canonical relation of R is given by

$$\begin{aligned} \mathcal{C} = \Big\{ \Big(&(E, \mathbf{x}_0), -\sigma q(r), -\sigma E q'(r)\boldsymbol{\omega}; (\mathbf{x}_0 + r\boldsymbol{\omega}, Eq(r)), \sigma E q'(r)\boldsymbol{\omega}, -\sigma \Big) \\ &: (E, \mathbf{x}_0) \in Y, r > 0, \boldsymbol{\omega} \in S^{n-2}, \sigma \neq 0 \Big\}. \end{aligned} \tag{3.11}$$

Proof. The proof rests on Lemma 3.3, which shows that $\Psi(E,\mathbf{x}_0,\mathbf{x}) = \widetilde{\Psi}(E,\mathbf{x}_0,\mathbf{x})$ in a neighborhood of $\mathcal{S}$. Because of this, Ψ and its derivatives are all the same as those of $\widetilde{\Psi}$ on $\mathcal{S}$. Therefore, for every $(E,\mathbf{x}_0) \in Y$ and $\mathbf{x} \in S(E,\mathbf{x}_0)$, $\Psi(E,\mathbf{x}_0,\mathbf{x}) = \widetilde{\Psi}(E,\mathbf{x}_0,\mathbf{x})$ *and* the weight $\left\|\nabla_{\mathbf{x}}\Psi\right\| = \left\|\nabla_{\mathbf{x}}\widetilde{\Psi}\right\|$ on $S(E,\mathbf{x}_0)$. Therefore, R can be written using $\widetilde{\Psi}$ instead of Ψ, resulting in

$$Rf(E,\mathbf{x}_0) = \int_{(\mathbf{x},x_n)\in X} f(\mathbf{x}',x_n)\left\|\nabla_{\mathbf{x}}\widetilde{\Psi}\right\|\delta\big(\widetilde{\Psi}(E,\mathbf{x}_0,(\mathbf{x}',x_n))\big)\mathrm{d}\mathbf{x}'\,\mathrm{d}x_n. \tag{3.12}$$

Using the Fourier transform representation of the delta function in x_n in (3.12), one gets (3.8) where $\widetilde{\Phi}$ and a are as given in (3.9) and (3.10), respectively. Because $\widetilde{\Psi}$ is smooth, the phase $\widetilde{\Phi}$ and the symbol a are both smooth. Since $\widetilde{\Psi} = 0$ only on $\mathcal{S}$, one shows the characteristic set of $\widetilde{\Phi}$ is the set where $\Psi = 0$, and it can be written using the coordinates indicated

$$Y \times (0,\infty) \times S^{n-2} \times \dot{\mathbb{R}} \ni \big((E,\mathbf{x}_0),(r,\boldsymbol{\omega}),\sigma\big) \mapsto \big((E,\mathbf{x}_0),(\mathbf{x}_0 + r\boldsymbol{\omega}, Eq(r)),\sigma\big) \in \Sigma_{\widetilde{\Psi}},$$

where we are using spherical coordinates on $\mathbb{R}^{n-1}$ and that $\frac{\partial\widetilde{\Phi}}{\partial\sigma} = \widetilde{\Psi} = \Psi$ on $\mathcal{S}$. In these coordinates $\mathrm{d}_{E,\mathbf{x}_0}\widetilde{\Psi} = \big(-\sigma q(r), -\sigma E q'(r)\boldsymbol{\omega}\big)$ and $\mathrm{d}_{\mathbf{x}}\widetilde{\Psi} = \big(-\sigma E q'(r)\boldsymbol{\omega},\sigma\big)$ on $\mathcal{S}$. This shows that $\widetilde{\Phi}$ is a nondegenerate phase function. These same calculations and Definition 2.3 show that the canonical relation of R is given by (3.11).

The symbol a is of order zero because it does not depend on σ. Since $\frac{\partial}{\partial x_n}\widetilde{\Psi} = 1$, a is also smooth and elliptic. Therefore, R is an elliptic FIO of order $O(R) = 0 + \frac{1}{2} - \frac{n}{2} = \frac{1-n}{2}$, using the formula of Definition 2.5. This finishes the proof. ∎

3.2. Proof of Theorem 3.1 in $\mathbb{R}^2$. We will first prove that R satisfies the semiglobal Bolker assumption in $\mathbb{R}^2$ as the proof in two dimensions is easier to follow than the general proof for $n \geq 3$, and as such we feel this provides a good introduction and outline to the main ideas of the $\mathbb{R}^n$ proof for a more general inverse problems audience (i.e., for readers not so familiar with microlocal analysis theory). After the result is proven in $\mathbb{R}^2$, we provide the general proof for $\mathbb{R}^n$.

Throughout this section, we use the coordinates $(E,x_0,\mathbf{x},\sigma) \in Y \times X \times \dot{\mathbb{R}}$, where $\mathbf{x} = (x_1,x_2)$. In this case, $S(E,x_0)$ consists of all points on the graph

$$\Psi(E,x_0,\mathbf{x}) = x_2 - Eq(|x_1 - x_0|) = 0,$$

(see (3.3)). Since $q(r) > 0$ when $r > 0$ and $q(0) = 0$, $S(E,x_0)$ consists of two disjoint connected curves in X, $x_2 = Eq((-1)^j(x_1 - x_0))$, $j = 1,2$, that are mirrors of each other in the vertical line $x_1 = x_0$. Their vertex is at $(x_0,0)$ which is not in X.

Define

$$D_j = D_j(x_0) = \big\{(x_1,x_2) : (-1)^j(x_1 - x_0) > 0, x_2 > 0\big\},$$

and let

$$\mathcal{D}_j = (0,\infty) \times \big\{(x_0,x_1) \in \mathbb{R}^2 : (-1)^j(x_1 - x_0) > 0\big\} \times \dot{\mathbb{R}}.$$

Then, one can write $\mathcal{C}$ as the disjoint union of $\mathcal{C}_1 \sqcup \mathcal{C}_2$ where, for $j = 1,2$,

$$\mathcal{C}_j = \Big\{\big((E,x_0), -\sigma q((-1)^j(x_1 - x_0)), (-1)^j\sigma E q'((-1)^j(x_1 - x_0));$$
$$\mathbf{x}, (-1)^j\sigma E q'((-1)^j(x_1 - x_0)), -\sigma\big) : (E,x_0,x_1,\sigma) \in \mathcal{D}_j, x_2 = Eq((-1)^j(x_1 - x_0))\Big\}.$$

In these coordinates using $\mathcal{D}_j$, the left projection $\Pi_L^{(j)} : \mathcal{D}_j \to \Pi_L^{(j)}(\mathcal{D}_j)$ is

$$\Pi_L^{(j)}(E, x_0, x_1, \sigma) = (E, x_0, -\sigma q((-1)^j(x_1 - x_0)), (-1)^j \sigma E q'((-1)^j(x_1 - x_0))).$$

Then the left projection $\Pi_L : \mathcal{D}_1 \sqcup \mathcal{D}_2 \to \Pi_L\big(\mathcal{D}_1 \sqcup \mathcal{D}_2\big)$ of R is defined by $\Pi_L = \Pi_L^{(1)}$ on $\mathcal{D}_1$, and $\Pi_L = \Pi_L^{(2)}$ on $\mathcal{D}_2$.

We will now show that condition 3.5 is equivalent to Π_L being an immersion. To do this we consider the derivatives of the $\Pi_L^{(j)}$,

$$D\Pi_L^{(j)} = \begin{pmatrix} 1 & 0 & 0 & 0 \\ 0 & 1 & 0 & 0 \\ a_{3,1} & a_{3,2} & (-1)^{j+1}\sigma q'((-1)^j(x_1 - x_0)) & -q((-1)^j(x_1 - x_0)) \\ a_{4,1} & a_{4,2} & \sigma E q''((-1)^j(x_1 - x_0)) & (-1)^j E q'((-1)^j(x_1 - x_0)) \end{pmatrix}. \tag{3.13}$$

The determinant is

$$\begin{aligned} \det D\Pi_L^{(j)} &= \det \begin{pmatrix} (-1)^{j+1}\sigma q'((-1)^j(x_1 - x_0)) & -q((-1)^j(x_1 - x_0)) \\ \sigma E q''((-1)^j(x_1 - x_0)) & (-1)^j E q'((-1)^j(x_1 - x_0)) \end{pmatrix} \\ &= \sigma E\big(q((-1)^j(x_1 - x_0))q''((-1)^j(x_1 - x_0)) - q'((-1)^j(x_1 - x_0))^2\big), \end{aligned} \tag{3.14}$$

which is nonvanishing if and only if

$$q(r)q''(r) - q'(r)^2 \neq 0 \quad \forall r > 0. \tag{3.15}$$

Now

$$g'(r) = \frac{q''(r)}{q(r)} - \frac{q'(r)^2}{q^2(r)} = 0 \iff q(r)q''(r) - q'(r)^2 = 0$$

for $x \in \dot{\mathbb{R}}$. The result follows.

We now show that condition (3.6) is equivalent to Π_L injective. We first consider the implication (3.6) $\implies$ Π_L injective.

Let g be injective, and let $(E_1, x_0, x_1, \sigma_1), (E_2, x_0', x_1', \sigma_2) \in \mathcal{D}_j$ be such that

$$\Pi_L^{(j)}(E_1, x_0, x_1, \sigma_1) = \Pi_L^{(j)}(E_2, x_0', x_1', \sigma_2).$$

Then $E_1 = E_2 = E$, $x_0 = x_0'$, and

$$\begin{pmatrix} -\sigma_1 q((-1)^j(x_1 - x_0)) \\ (-1)^j \sigma_1 E q'((-1)^j(x_1 - x_0)) \end{pmatrix} = \begin{pmatrix} -\sigma_2 q((-1)^j(x_1' - x_0)) \\ (-1)^j \sigma_2 E q'((-1)^j(x_1' - x_0)) \end{pmatrix}. \tag{3.16}$$

It follows that

$$(-1)^{j-1} E g((-1)^j(x_1 - x_0)) = (-1)^{j-1} E g((-1)^j(x_1' - x_0)).$$

Hence $x_1 = x_1'$, for $j = 1, 2$, since $E > 0$ and g is injective. Now $\sigma_1 q((-1)^j(x_1 - x_0)) = \sigma_2 q((-1)^j(x_1 - x_0)) \implies \sigma_1 = \sigma_2$ since $q((-1)^j(x_1 - x_0)) > 0$ on $\mathcal{D}_j$. Thus, $\Pi_L^{(j)}$ is injective for $j = 1, 2$.

Now let $(E_1, x_0, x_1, \sigma_1) \in \mathcal{D}_1$ and $(E_2, x_0', x_1', \sigma_2) \in \mathcal{D}_2$ be such that $\Pi_L^{(1)}(E_1, x_0, x_1, \sigma_1) = \Pi_L^{(2)}(E_2, x_0', x_1', \sigma_2)$. Then $E_1 = E_2 = E$, $x_0 = x_0'$, and

$$\begin{pmatrix} -\sigma_1 q(-(x_1 - x_0)) \\ -\sigma_1 E q'(-(x_1 - x_0)) \end{pmatrix} = \begin{pmatrix} -\sigma_2 q(x_1' - x_0) \\ \sigma_2 E q'(x_1' - x_0) \end{pmatrix}. \tag{3.17}$$

Thus it follows that

$$g(-(x_1 - x_0)) = -g(x_1' - x_0). \tag{3.18}$$

Now $x_1 - x_0 < 0$ on $\mathcal{D}_1$ and $x_1' - x_0 > 0$ on $\mathcal{D}_2$. Further $g(r) > 0$ for all $r > 0$ by assumption, so (3.18) is impossible. Hence Π_L is injective on $\mathcal{C}$.

We now prove the converse implication, namely Π_L injective $\implies$ (3.6). Let g be noninjective, and let $r_1, r_2 \in (0, \infty)$ be such that $g(r_1) = g(r_2)$, with $r_1 \neq r_2$. We have $\Pi_L^{(j)}(E, x_0, x_1, \sigma_1) = \Pi_L^{(j)}(E, x_0, x_1', \sigma_2) \iff$ (3.16) holds. We can write (3.16) as

$$A\boldsymbol{\sigma} = \begin{pmatrix} q((-1)^j(x_1 - x_0)) & -q((-1)^j(x_1' - x_0)) \\ (-1)^{j-1} q'((-1)^j(x_1 - x_0)) & (-1)^j q'((-1)^j(x_1' - x_0)) \end{pmatrix} \begin{pmatrix} \sigma_1 \\ \sigma_2 \end{pmatrix} = \begin{pmatrix} 0 \\ 0 \end{pmatrix}.$$

The determinant of A is

$$\det(A) = (-1)^j \big(q'((-1)^j(x_1' - x_0)) q((-1)^j(x_1 - x_0)) - q((-1)^j(x_1' - x_0)) q'((-1)^j(x_1 - x_0)) \big).$$

Thus setting $x_1 = x_0 + (-1)^j r_1$ and $x_1' = x_0 + (-1)^j r_2$ (note $x_1 \neq x_1'$) yields $\det(A) = 0$, since

$$g(r_1) = g(r_2) \implies \frac{q'(r_1)}{q(r_1)} = \frac{q'(r_2)}{q(r_2)} \implies q'(r_1) q(r_2) = q'(r_2) q(r_1).$$

Hence there exist $\sigma_1, \sigma_2 \neq 0$, such that $\boldsymbol{\sigma} \in \operatorname{null}(A)$. For example, $\sigma_1 = 1$ and

$$\sigma_2 = \frac{\sqrt{q^2(r_1) + q'(r_1)^2}}{\sqrt{q^2(r_2) + q'(r_2)^2}} \neq 0$$

is sufficient. Therefore Π_L is noninjective. Finally, (3.5) $\implies$ (3.6) (see Remark 3.2), so condition (3.5) is equivalent to the semiglobal Bolker assumption. This completes the proof.

Remark 3.5. When g is noninjective, Π_L is noninjective (see Remark 3.2) and artifacts can be generated. Using (3.11) one can show that $\mathcal{C}^t \circ \mathcal{C} \subset \Delta \cup \Lambda$, where Δ is the diagonal in $T^*X \times T^*X$ and $\Lambda \subset T^*X \times T^*X$. This is important because if $\lambda \in \mathrm{WF}(f)$, then

$$\mathcal{C}^t \circ \mathcal{C} \circ \{\lambda\} \subset \big(\Delta \circ \{\lambda\}\big) \cup \big(\Lambda \circ \{\lambda\}\big) = \{\lambda\} \cup \big(\Lambda \circ \{\lambda\}\big),$$

and by the Hörmander–Sato lemma both a visible singularity at λ and an artifact at $\Lambda \circ \{\lambda\}$ could be in $\mathrm{WF}(R^* \psi R f)$ (where ψ is a cutoff to make $R^* \psi R$ defined).

To describe the artifacts and, implicitly, Λ, there are no artifacts if R satisfies (3.5) in Theorem 3.1 since, in this case R^*R is a PDO. We will now analyze possible artifacts if R does not satisfy this condition. This means that

$$\begin{aligned} \mathcal{C}^t \circ \mathcal{C} &= (\mathcal{C}_1 \cup \mathcal{C}_2)^t \circ (\mathcal{C}_1 \cup \mathcal{C}_2) \\ &= (\mathcal{C}_1^t \circ \mathcal{C}_1) \cup (\mathcal{C}_2^t \circ \mathcal{C}_2) \cup (\mathcal{C}_2^t \circ \mathcal{C}_1) \cup (\mathcal{C}_1^t \circ \mathcal{C}_2) \\ &= (\mathcal{C}_1^t \circ \mathcal{C}_1) \cup (\mathcal{C}_2^t \circ \mathcal{C}_2). \end{aligned} \tag{3.19}$$

The cross terms disappear because $\mathcal{C}_j^t \circ \mathcal{C}_i = \emptyset$ as $\mathcal{D}_i \cap \mathcal{D}_j = \emptyset$, regardless of the conditions of Theorem 3.1. Therefore, any artifacts are due to the $\mathcal{C}_j^t \circ \mathcal{C}_j \subset \Delta \cup \Lambda$ for $j = 1, 2$. Also, in the case when the conditions of Theorem 3.1 are not satisfied, the matrix in (3.13) drops rank by 1, and hence the projections Π_L and Π_R have singularities (e.g., of type fold or blowdown [9]) of order 1 on $\{g' = 0\}$ (see [9, Definition 2.6]). In the next paragraph we provide implicit expressions for the artifacts caused by the $\{g' = 0\}$ singularities in the case when the conditions of Theorem 3.1 are not satisfied.

Let us assume g is not injective. We can choose $r_1 \neq r_2$ such that $g(r_1) = g(r_2)$. Let f be a distribution and assume for some (E, x_0, σ_1),

$$\lambda = \big((x_0 + (-1)^j r_1, Eq((-1)^j r_1)), \sigma_1 Eq'((-1)^j r_1), -\sigma_1\big) \in \mathrm{WF}(f).$$

Equivalently, assume there exists an integration curve which intersects a singularity of f normal to its direction. Then, one can choose a $\sigma_2 \in \dot{\mathbb{R}}$ such that $\Pi_L(E, x_0, r_1, \sigma_1) = \Pi_L(E, x_0, r_2, \sigma_2)$ where we are using the coordinates above (3.16). This is true because the ratio $g = q'/q$ is the same at r_1 and r_2. Then by calculating $\mathcal{C}_j^t \circ \mathcal{C}_j \circ \{\lambda\}$ and using the Hörmander–Sato lemma, one sees that R^*Rf could have an artifact at $(x_0 + (-1)^j r_2, Eq(r_2)$, $\sigma_2(-1)^j Eq'(r_2), -\sigma_2)$, and this implicitly describes Λ. Note that artifacts can occur for either $\mathcal{C}_j$. These artifacts will be shown in simulations in Example 4.3.

3.3. Proof of Theorem 3.1 in $\mathbb{R}^n$.

Proof. Corollary 3.4 shows that R is an FIO and gives its canonical relation $\mathcal{C}$ in equation (3.11). We now investigate $\Pi_L : \mathcal{C} \to T^*(Y)$ to show that R satisfies the semiglobal Bolker assumption.

Note that $(E, \mathbf{x}_0, r, \boldsymbol{\omega}, \sigma) \in Y \times (0, \infty) \times S^{n-2} \times \dot{\mathbb{R}}$ give coordinates on $\mathcal{C}$. In these coordinates, Π_L becomes

$$\begin{aligned} (E, \mathbf{x}_0, r, \boldsymbol{\omega}, \sigma) &\mapsto (E, \mathbf{x}_0, -\sigma q(r), -\sigma Eq'(r)\boldsymbol{\omega}) = (E, \mathbf{x}_0, \eta, \boldsymbol{\xi}), \\ &\text{where} \quad \eta = -\sigma q(r) \in \dot{\mathbb{R}}, \quad \boldsymbol{\xi} = -\sigma Eq'(r)\boldsymbol{\omega} \in \mathbb{R}^{n-1}. \end{aligned} \tag{3.20}$$

Let $\boldsymbol{\lambda} = (E, \mathbf{x}_0, \eta, \boldsymbol{\xi})$ be in the image of Π_L. Then (3.20) gives $(E, \mathbf{x}_0)$ and we need to find formulas for r, $\boldsymbol{\omega}$, and σ in terms of $\boldsymbol{\lambda}$. Recall that we have defined $g(r) = q'(r)/q(r)$. By assumption, $g : (0, \infty) \to (0, \infty)$ and $q(r) > 0$ on $(0, \infty)$, so q' is always positive on $(0, \infty)$. This explains why η and $\boldsymbol{\xi}$ are nonzero.

Let

$$\mathbf{w} = \frac{1}{E\eta}\boldsymbol{\xi} = g(r)\boldsymbol{\omega};$$

then $\mathbf{w}$ is known from (3.20) as is $\|\mathbf{w}\| = g(r)$.

First, assume g is injective. Then, r is determined and $q(r)$ is known and so

$$\sigma = \frac{-\eta}{q(r)}, \qquad \boldsymbol{\omega} = \frac{-1}{\sigma Eq'(r)}\boldsymbol{\xi} \tag{3.21}$$

are determined from $(E, \mathbf{x}_0, \eta, \boldsymbol{\xi})$ using (3.20). Therefore, Π_L is injective. Next, if g is not injective, then for multiple values of r, (3.20) maps to the same point and Π_L is not injective. Therefore, g is injective if and only if Π_L is.

To prove Π_L is an immersion if and only if g' is never zero, one does a calculation similar to the calculations in (3.13)–(3.15). The calculation is simplified by choosing orthonormal coordinates on S^{n-2} at $\boldsymbol{\omega}$. Extend $\boldsymbol{\omega}$ to an orthonormal basis of $\mathbb{R}^{n-1}$: $\{\omega, \omega_1, \omega_2, \ldots, \omega_{n-2}\}$; then the directional derivatives ∇_{ω_j} in direction ω_j, $j = 1, 2, \ldots, n-2$, form an orthonormal basis of tangent vectors on S^{n-2} at ω. Let $I(\boldsymbol{\omega}) = \boldsymbol{\omega}$ be the identity function on S^{n-2}. A straightforward calculation shows that $\nabla_{\omega_j} I(\omega) = \omega_j$. This simplifies the calculation of the determinant $\det D\Pi_L$, which reduces, for fixed (E, x_0), to calculating the determinant of the derivative of the map

$$(r, \boldsymbol{\omega}, \sigma) \mapsto \begin{pmatrix} \sigma q(r) \\ \sigma q'(r)\boldsymbol{\omega} \end{pmatrix}.$$

The derivative matrix is

$$\begin{pmatrix} \sigma q'(r) & 0 & 0 & \cdots & 0 & q(r) \\ \sigma q''(r)\boldsymbol{\omega} & \sigma q'(r)\boldsymbol{\omega}_1 & \sigma q'(r)\boldsymbol{\omega}_2 & \cdots & \sigma q'(r)\boldsymbol{\omega}_{n-2} & q'(r)\boldsymbol{\omega} \end{pmatrix}.$$

Note that we are viewing $\boldsymbol{\omega}$ and $\boldsymbol{\omega}_j$ as column vectors. By expanding on the first row and using orthogonality of $\{\boldsymbol{\omega}, \boldsymbol{\omega}_1, \ldots, \boldsymbol{\omega}_{n-2}\}$, one sees, since $\eta \neq 0$ and therefore $\sigma \neq 0$ in (3.21), that $\det D\Pi_L \neq 0$ if and only if

$$(q'(r))^{n-2} \left[q(r)q''(r) - \left(q'(r)\right)^2 \right] \neq 0,$$

and this expression is nonzero if and only if g' is never zero on $(0, \infty)$.

Finally, as noted in Remark 3.2, condition (3.5) implies condition (3.6), so condition (3.5) is equivalent to the semiglobal Bolker assumption. ∎

3.4. Sobolev smoothness. In this section we describe the microlocal continuity properties of R. Then, we analyze visible and invisible features in a filtered backprojection reconstruction operator (see (3.28)). By *visible feature* we mean a wavefront singularity of a function that appears in its reconstruction, and by *invisible feature*, we mean a wavefront singularity of a function that does not appear as a wavefront singularity in the reconstruction.

We will use Sobolev norms and microlocal Sobolev wavefront sets to analyze the level of smoothing that a Radon transform applies to the object. This smoothing indicates the stability of the inverse of the Radon transform (which has to "unsmooth" the data). The more the Radon transform smooths, the more the inverse has to "unsmooth" and the more highly ill-posed inversion becomes (particularly in regard to edge recovery), and vice versa. For example, the hyperplane (X-ray CT) Radon transform applies order $(n-1)/2$ smoothing in Sobolev scale (a relatively low-level smoothing) in n-dimensions, and can be inverted stably for low n with only minor regularization. Thus, Sobolev estimates on how much an operator smooths are a powerful tool for analyzing the stability of Radon transforms. We will show in this section that the level of smoothing of the generalized cone transform is $(n-1)/2$, in n-dimensions (the same as the hyperplane Radon transform).

We use Sobolev wavefront sets to analyze the strength of visible singularities. These visible singularities tell us which edge directions the Radon transform can image stably, and thus provide additional, more specific, information about the transform's stability. We make this precise in Theorem 3.12, in which we describe how much each visible singularity of the

original function is emphasized in Sobolev scale by a lambda-filtered backprojection operator, (3.28).

Now, we introduce Sobolev spaces and Sobolev wavefront sets [31, 34].

Definition 3.6. *Let $\alpha \in \mathbb{R}$. Then $H^\alpha(\mathbb{R}^n)$ is the set of all distributions for which their Fourier transform is a locally integrable function and such that the Sobolev norm*

$$\|f\|_\alpha = \Big(\int_{\boldsymbol{\xi}\in\mathbb{R}^n} |\mathcal{F}(f)(\boldsymbol{\xi})|^2 \left(1 + \|\boldsymbol{\xi}\|^2\right)^\alpha \mathrm{d}\boldsymbol{\xi} \Big)^{1/2} < \infty. \tag{3.22}$$

Let $\Omega \subset \mathbb{R}^n$. Then, $H^\alpha(\Omega)$ will be the set of all distributions in $H^\alpha(\mathbb{R}^n)$ that are supported in Ω, and $H_c^\alpha(\Omega)$ will be all those of compact support in Ω. We define $H_{loc}^\alpha(\Omega)$ as the set of all distributions f supported in Ω such that for each $\varphi \in \mathcal{D}(\Omega)$, the product $\varphi f \in H^\alpha(\mathbb{R}^n)$.

We give $H_c^\alpha(\Omega)$ the topology using the Sobolev norm (so $H_c^\alpha(\Omega)$ is not closed), and we give $H_{\mathrm{loc}}^\alpha(\Omega)$ the topology defined by the seminorms $\|f\|_{\alpha,\varphi} = \|\varphi f\|_\alpha$ (so $H_{\mathrm{loc}}^\alpha(\Omega)$ is metrizable).

Definition 3.7. *Let $m \in \mathbb{R}$, and let Ω' be an open set in $\mathbb{R}^n$. Then, the linear map $F : H_c^\alpha(\Omega) \to H_{loc}^{\alpha-m}(\Omega')$ is continuous if for each $\varphi \in \mathcal{D}(\Omega)$ and $\tilde{\varphi} \in \mathcal{D}(\Omega')$ the product map $\tilde{\varphi}\, F\, \varphi$ is continuous from $H^\alpha(\Omega)$ to $H^{\alpha-m}(\Omega')$ in Sobolev norms.*

Corollary 3.8. *Let q satisfy (3.1) as well as condition (3.5) of Theorem 3.1. Then R is continuous from $H_c^\alpha(X)$ to $H_{loc}^{\alpha+(n-1)/2}(Y)$.*

This corollary indicates that the forward map is stable in Sobolev scale $\frac{1-n}{2}$, in the sense that we can obtain bounds of the form $\|\tilde{\varphi}Rf\|_{H^{\alpha+(n-1)/2}(Y)} \le C\|\varphi f\|_{H^\alpha(X)}$ for every $\alpha \in \mathbb{R}$ and $n \ge 2$, where C is constant depending on α n, $\varphi \in \mathcal{D}(X)$, and $\tilde{\varphi} \in \mathcal{D}(Y)$.

Proof. The operator R is an FIO of order $\frac{1-n}{2}$ with immersive left projection and for each $\tilde{\varphi}$ and φ in Definition 3.7, the operator $\tilde{\varphi}R\varphi$ is compactly supported. Therefore, [17, Theorem 4.3.1] can be used to show R is continuous according to Definition 3.7 from H_c^α to $H_{\mathrm{loc}}^{\alpha+(n-1)/2}$. ∎

We now define the Sobolev wavefront set [31]. This will provide the language to describe the strength of the visible singularities in Sobolev scale.

Definition 3.9. *Let $\alpha \in \mathbb{R}$, and let $X \subset \mathbb{R}^n$. Let $f \in \mathcal{D}'(X)$, and let $(\mathbf{x}, \boldsymbol{\xi}) \in X \times \dot{\mathbb{R}}^n$. Then, f is* (Sobolev) smooth to order α at $(\mathbf{x}, \xi)$ *if there are a smooth cutoff function φ at $\mathbf{x}_0$ and a conic neighborhood V of $\boldsymbol{\xi}$ such that*

$$\int_{\boldsymbol{\eta}\in V} |\mathcal{F}(\varphi f)(\boldsymbol{\eta})|^2 \left(1 + \|\boldsymbol{\eta}\|^2\right)^\alpha \mathrm{d}\boldsymbol{\eta} < \infty. \tag{3.23}$$

If f is not smooth to order α at $(\mathbf{x}, \boldsymbol{\xi})$, then $(\mathbf{x}, \boldsymbol{\xi})$ is in the Sobolev wavefront set $\mathrm{WF}^\alpha(f)$.

If V were replaced by $\mathbb{R}^n$ in the integral (3.23), then boundedness of the integral would mean that φf is in H^α. By restricting the integral to be over V we require φf to be in H^α *only* in some conic neighborhood of $\boldsymbol{\xi}$. This is a Sobolev equivalent of Definition 2.1 for C^∞ wavefront set: rapid decrease in V of the localized Fourier transform is replaced with finite Sobolev seminorm in V.

Our next theorem gives the precise relationship between Sobolev singularities of f and those of Rf.

Theorem 3.10. *Assume $q : [0,\infty) \to [0,\infty)$ satisfies (3.1) and (3.5). Let R be the associated generalized cone Radon transform. Let $(\mathbf{x},\boldsymbol{\xi}) \in \mathbb{R}^n \times \dot{\mathbb{R}}^n$ and assume that $\boldsymbol{\xi}' \neq \mathbf{0}$ and $\xi_n \neq 0$. Then,*

$$(\mathbf{x},\boldsymbol{\xi}) \in \mathrm{WF}^{\alpha}(f) \quad \Longleftrightarrow \quad \left(E, \mathbf{x}_0, -\sigma q(r), -\sigma E q'(r)\boldsymbol{\omega}\right) \in \mathrm{WF}^{\alpha+(n-1)/2}(Rf), \tag{3.24}$$

where

$$\begin{aligned} &\boldsymbol{\omega} = -\tfrac{\xi_n}{|\xi_n|}\tfrac{\boldsymbol{\xi}'}{\left\|\boldsymbol{\xi}'\right\|}, && r = g^{-1}\Big(\tfrac{\left\|\boldsymbol{\xi}'\right\|}{x_n|\xi_n|}\Big), && \sigma = -\xi_n. \\ &E = \tfrac{x_n}{q(r)}, && \mathbf{x}_0 = \mathbf{x}' - r\boldsymbol{\omega}. \end{aligned} \tag{3.25}$$

In general, Radon transforms make singularities somewhat smoother (see [32, Theorem 3.1]). Theorem 3.10 shows that every singularity of f generates a singularity of Rf in a specific wavefront direction that is $(n-1)/2$ degrees smoother in Sobolev scale. Every $(\mathbf{x},\boldsymbol{\xi}) \in \mathrm{WF}^{\alpha}(f)$ with $\boldsymbol{\xi}' \neq \mathbf{0}$ and $\xi_n \neq 0$ will create a specific singularity in $\mathrm{WF}^{\alpha+(n-1)/2}(Rf)$ given by (3.25). Our proof, in particular (3.26), will show that Π_R is injective.

Remark 3.11. Vertical and horizontal covectors $(\mathbf{x},\boldsymbol{\xi}) \in \mathrm{WF}(f)$ (where $\boldsymbol{\xi}' = \mathbf{0}$, respectively, $\xi_n = 0$) will not create singularities in Rf. Therefore, they will be invisible in any reconstruction when the reconstruction operator is an FIO.

The reason is as follows. For a singularity $(\mathbf{x},\boldsymbol{\xi})$ to be visible in Rf, it must be in the image $\Pi_R(\mathcal{C})$ because

$$\mathrm{WF}(Rf) = \mathcal{C} \circ \mathrm{WF}(f) = \Pi_L \circ \Pi_R^{-1}(\mathrm{WF}(f))$$

by ellipticity, the semiglobal Bolker assumption, and the Hörmander–Sato lemma (Theorem 2.6). For $(\mathbf{x},\boldsymbol{\xi})$ to be in the image of Π_R, $\boldsymbol{\xi}' = \sigma E q'(r)\boldsymbol{\omega}$ must be nonzero, and this explains why no vertical covector is in the image of Π_R. Furthermore, $\xi_n = -\sigma$ must be nonzero, and this explains why no horizontal covector generates a singularity in Rf.

Therefore, one would expect that those singularities, such as vertical or horizontal object boundaries, would be difficult to image in reconstruction methods. For filtered backprojection reconstruction methods, this follows from the proof of Theorem 3.12.

Proof of Theorem 3.10. By the Hörmander–Sato lemma (Theorem 2.6), $\mathrm{WF}(Rf) \subset \mathcal{C} \circ \mathrm{WF}(f)$. If R is elliptic and satisfies the semiglobal Bolker assumption, then the equality holds: The $\subset$ inequality follows from the Hörmander–Sato lemma applied to R, and the $\supset$ containment follows from the Hörmander–Sato lemma applied microlocally to microlocally elliptic local parametrices to R (operators that microlocally invert R, i.e., recover singularities microlocally; see, e.g., [17]).

The Sobolev version of this wavefront equality follows from Sobolev continuity of R and of this microlocal parametrix; the proof is given in [33] and [3, Proposition A.6] for the classical Radon transform. That proof just uses Sobolev continuity of the classical transform, so it can be adapted with essentially the same arguments to our case with Sobolev continuity of order $\frac{1-n}{2}$ (see [31, Corollary 6.6] for the pseudodifferential case). This allows us to say that

$$\mathcal{C} \circ \left(\mathrm{WF}^{\alpha}(f) \cap \Pi_R(\mathcal{C})\right) = \mathrm{WF}^{\alpha+(n-1)/2}(Rf).$$

To finish the proof of Theorem 3.10, we analyze Π_R in the coordinates $(E, \mathbf{x}_0, r, \boldsymbol{\omega}, \sigma) \in Y \times (0,\infty) \times S^{n-2} \times \dot{\mathbb{R}}$ used in Theorem 3.1. In these coordinates the map Π_R is described by

$$(E, \mathbf{x}_0, r, \boldsymbol{\omega}, \sigma) \mapsto \big((\mathbf{x}_0 + r\boldsymbol{\omega}, Eq(r)), \sigma E q'(r)\boldsymbol{\omega}, -\sigma\big) = (\mathbf{x}, \boldsymbol{\xi}). \tag{3.26}$$

If one solves (3.26), for $(E, \mathbf{x}_0, r, \boldsymbol{\omega}, \sigma)$ one gets (3.25), and therefore,

$$(E, \mathbf{x}_0, -\sigma q(r), -\sigma E q'(r)\boldsymbol{\omega}) = \Pi_L \circ \Pi_R^{-1}(\mathbf{x}, \boldsymbol{\xi}) = \mathcal{C} \circ (\mathbf{x}, \boldsymbol{\xi}). \qquad \blacksquare$$

We will now consider the problem in $\mathbb{R}^2$, and let $\mathbf{x} = (x_1, x_2)$ denote a point in $\mathbb{R}^2$. One of the reconstruction methods in the next section is a truncated lambda-filtered back-projection (FBP) using data for (E, x_0) in a rectangle

$$\mathcal{A} := [a, b] \times [-c, c], \tag{3.27}$$

where $0 < a < b$ and $0 < c$. Let $\chi_{\mathcal{A}}$ be the characteristic function of $\mathcal{A}$. The generalized lambda reconstruction method we use for functions in $\mathbb{R}^2$ is

$$\mathcal{L}f := R^*\left(\chi_{\mathcal{A}} \frac{\mathrm{d}^2}{\mathrm{d}E^2} Rf\right). \tag{3.28}$$

To connect this to reconstructions we need to understand what singularities of f are visible in its reconstruction from $\mathcal{L}$. An analysis of added artifacts will be done elsewhere.

Theorem 3.12 (visible singularities for $\mathcal{L}$ in $\mathbb{R}^2$). *Assume $q : [0,\infty) \to [0,\infty)$ satisfies (3.1) and (3.5). Let R be the associated generalized cone Radon transform in $\mathbb{R}^2$. Let $\alpha \in \mathbb{R}$, and let $\mathcal{L}$ be given by (3.28). Let $f \in \mathcal{E}'(X)$ and $(\mathbf{x}, \boldsymbol{\xi}) \in \mathrm{WF}^{\alpha}(f)$. Then, $(\mathbf{x}, \boldsymbol{\xi}) \in \mathrm{WF}^{\alpha-1}(\mathcal{L}f)$ if*

1. *$\xi_1 \neq 0$ and $\xi_2 \neq 0$ and*
2. *$\frac{x_2}{q(r)} \in (a, b)$ and $x_1 - r\omega \in (-c, c)$, where $r = g^{-1}\big(\frac{|\xi_1|}{x_2|\xi_2|}\big)$ and $\omega = -\frac{\xi_1\xi_2}{|\xi_1\xi_2|}$.*

If $(\mathbf{x}, \boldsymbol{\xi})$ does not satisfy condition (1), or it does satisfy (1) but $\frac{x_2}{q(r)} \notin [a, b]$, or $x_1 - r\omega \notin [-c, c]$, then $\mathcal{L}f$ will be smooth at $\mathbf{x}$ in direction $\boldsymbol{\xi}$.

Remark 3.13. Note that Theorems 3.10 and 3.12 are valid for all Radon transforms defined on surfaces $S(E, \mathbf{x}_0)$ for which q and g satisfy the conditions in Theorem 3.1 and the weights on the surfaces are smooth and nowhere zero.

The reconstructions in section 4 show the visible singularities and the invisible singularities predicted by Theorem 3.12. For a visualization of the visible singularities with broken-ray data (i.e., when $q(r) = r$), see Figure 2. The range of x_0 and E used is chosen to be consistent with the simulations conducted in section 4. We notice a greater directional coverage for $\mathbf{x}$ close to $\{x_2 = 0\}$, and conversely for $\mathbf{x}$ moving away from $\{x_2 = 0\}$.

Note that this theorem does not say anything about singularities of $\mathcal{L}f$ for $(\mathbf{x}, \boldsymbol{\xi}) \in \mathrm{WF}(f)$ for which $\frac{x_2}{q(r)} \in \{a, b\}$, or $x_1 - r\omega = \pm c$. Singularities at these wavefront directions are more complicated to analyze and artifacts can be created because of these points. These so-called boundary artifacts are seen in Figure 3; the boundary points in the data set labeled "Edge 1" and "Edge 2" in Figure 3a are points in the support of $R\delta$ at the boundary of the data set, $\mathcal{A}$. Then, you can see the artifacts they create (labeled the same way) in Figure 3c. Similar artifacts are highlighted in the sinogram in Figure 3d along with the resulting artifacts in Figure 3f. These artifacts are predicted by the microlocal analysis of the operator $\mathcal{L}$, and a more thorough analysis of such artifacts will appear elsewhere.

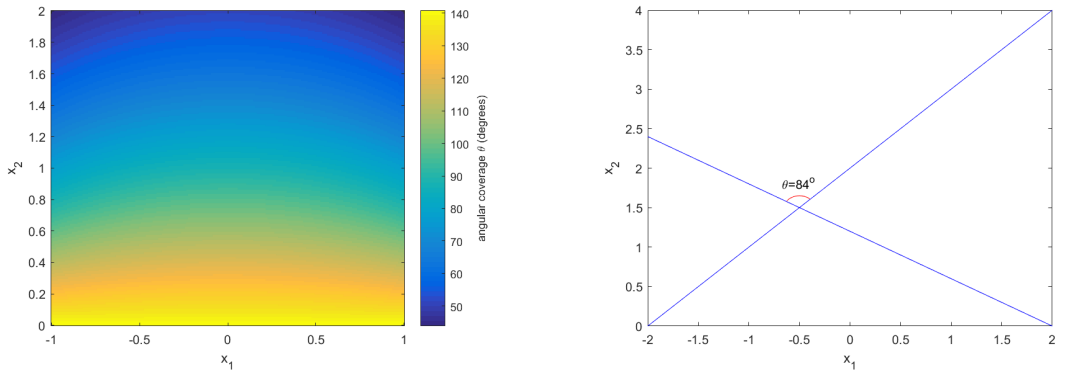

(a) θ coverage. (b) Example θ.

Figure 2. *Left: Set of angular coverage (θ) with broken-ray data on $[-2,2]\times[0,2]$ for $x_0\in[-2,2]$ and $E\in(0,2.83]$ (i.e., when $c=2$, $a=0$, and $b=2.83$). Right: Example θ for the point $(-0.5,1.5)$. The set of directions resolved by the data (ξ) is the red cone displayed in the right-hand figure, rotated by 90° about $(-0.5,1.5)$, minus the direction $\xi=(1,0)$.*

Proof. Let $(\mathbf{x},\boldsymbol{\xi})\in \mathrm{WF}^{\alpha}(f)$. First, assume that condition (1) in this theorem holds. Then, by Theorem 3.10,

$$\boldsymbol{\lambda}=(E,\mathbf{x}_0,-\sigma q(r),-\sigma E q'(r)\boldsymbol{\omega})\in \mathrm{WF}^{\alpha+1/2}(Rf)$$

by (3.25) where $r=g^{-1}\big(\frac{|\xi_1|}{x_2|\xi_2|}\big)$ and $\omega=-\frac{\xi_1\xi_2}{|\xi_1\xi_2|}$, $E=\frac{x_2}{q(r)}$, and $x_0=x_1-r\omega$. Since $\frac{\mathrm{d}^2}{\mathrm{d}E^2}$ is elliptic of order two in this direction, $\boldsymbol{\lambda}\in \mathrm{WF}^{\alpha-3/2}\big(\frac{\mathrm{d}^2}{\mathrm{d}E^2}Rf\big)$.

If condition (2) of this theorem holds, then $(E,x_0)\in\mathrm{int}(\mathcal{A})$, the interior of $\mathcal{A}$, and since $\chi_{\mathcal{A}}$ is one in a neighborhood of (E,x_0), $\boldsymbol{\lambda}\in \mathrm{WF}^{\alpha-3/2}\big(\chi_{\mathcal{A}}\frac{\mathrm{d}^2}{\mathrm{d}E^2}Rf\big)$. Because R^* is elliptic of order $-1/2$ and satisfies the semiglobal Bolker assumption, $(\mathbf{x},\xi)=\mathcal{C}^t\circ\{\boldsymbol{\lambda}\}$ is in $\mathrm{WF}^{\alpha-1}(\mathcal{L}f)$. This statement is proven for R^* using the similar arguments to the analogous statement for R at the start of the proof of Theorem 3.10.

Next, if condition (1) of this theorem holds but $\frac{x_2}{q(r)}\notin[a,b]$, or $x_1-r\omega\notin[-c,c]$, then (E,x_0) is in the exterior of $\mathcal{A}$ and so $\chi_{\mathcal{A}}\frac{\mathrm{d}^2}{\mathrm{d}E^2}Rf$ is zero, hence smooth in a neighborhood of (E,x_0). Since R^* is an FIO with canonical relation $\mathcal{C}^t$, $(\mathbf{x},\boldsymbol{\xi})=\mathcal{C}^t\circ\boldsymbol{\lambda}\notin \mathrm{WF}(\mathcal{L}f)$.

Finally, if (1) does not hold, then, as discussed in Remark 3.11, $(\mathbf{x},\boldsymbol{\xi})$ does not create any singularity in Rf and therefore not in $\mathcal{L}f$ (i.e., $\mathcal{C}\circ\{(\mathbf{x},\boldsymbol{\xi})\}=\emptyset$ and so $\mathcal{C}^t\circ\mathcal{C}\circ\{(\mathbf{x},\boldsymbol{\xi})\}=\emptyset$). This finishes the proof. ∎

4. Examples in $\mathbb{R}^2$ and reconstructions.

In this section we analyze several examples to provide perspective on our results. We present reconstructions by inverse crime (noise level zero) to verify our theory. We note in each case if the conditions of Theorem 3.1 (equivalently Bolker) are satisfied.

Example 4.1 (CST: Bolker satisfied). Some simple examples of interest are the monomials

$$q(r)=r^{\alpha}, \tag{4.1}$$

where $\alpha > 0$. In this case $g(r) = \frac{\alpha r^{\alpha-1}}{r^\alpha} = \frac{\alpha}{r}$, which is injective on $(0,\infty)$, and $g'(r) = -\frac{\alpha}{r^2}$, which is never zero. Hence the conditions of Theorem 3.1 are satisfied and the generalized Radon integrals satisfy the semiglobal Bolker assumption. A specific monomial of interest in X-ray CT and CST is the straight line $q_C(r) = r$, when $\alpha = 1$. In this case, R reduces to the broken-ray transforms of [2, 5] in gamma ray source imaging in CST. See Figure 1 for an example of broken-ray integration curves when $x_0 = 3$ and $E = 0.5$. Let $B = \{(x,y) \in \mathbb{R}^2 : x^2 + (y-1)^2 < 0.2^2\}$. Then, see Figure 3 for reconstructions of a delta function $f = \delta$, centered at $(0,1)$, and disc phantom $f = \chi_B$ from Rf, when $q = q_C$. The scanning region used is $[-1,1] \times [0,2]$, and we simulate $Rf(E, x_0)$ for $E \in (0, 2.83)$ and $x_0 \in [-2,2]$. The delta function is simulated as a characteristic function on a square with small area. That is, $\delta \approx \chi_S$, where $S = [-0.015, 0.015] \times [0.985, 1.015]$ (i.e., a 3×3 pixel grid centered AT $(0,1)$). The reconstruction methods used are FBP (see Figures 3b and 3e and Remark 3.13) using $\frac{\mathrm{d}^2}{\mathrm{d}E^2}$ as a filter, and Landweber iteration (see Figures 3c and 3f). Note the difference in scales of the color bars between Figures 3b and 3c, and 3e and 3f. The aim of the generalized lambda reconstruction (3.28) is to recover the image singularities, and the reconstructed values give primarily qualitative information. Therefore, these color bar ranges of Figures 3b and 3e are chosen to show the singularities of the object. The Landweber iteration approximates the exact solution numerically, and thus the color bar ranges of Figures 3c and 3f more closely represent the original density range (i.e., $[0,1]$ for the phantoms considered).

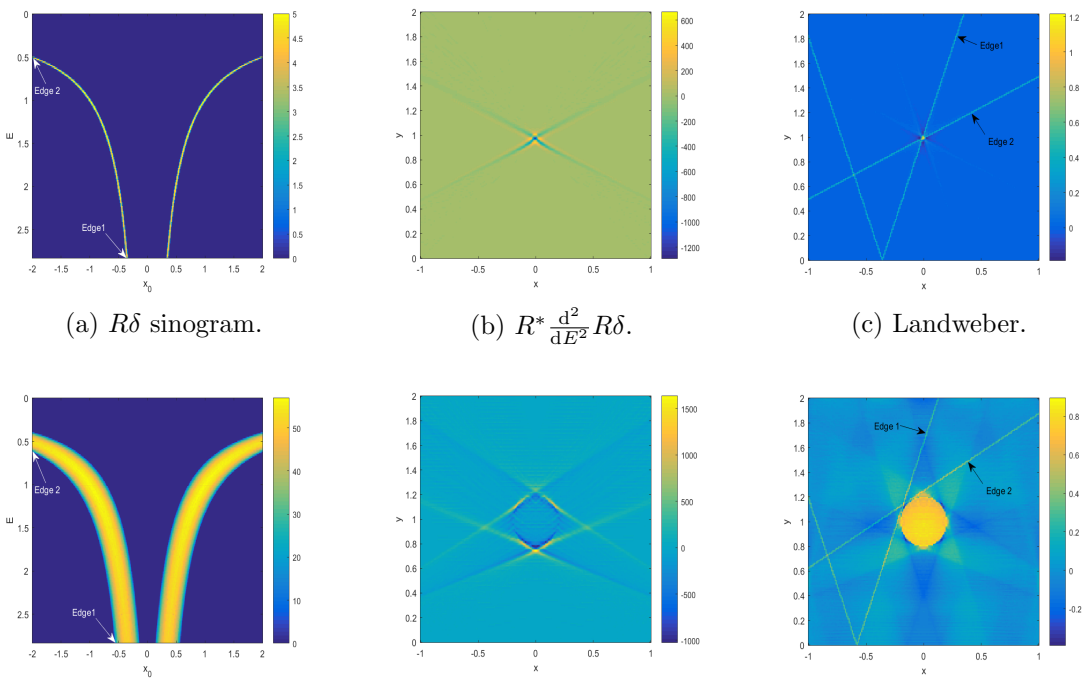

(a) $R\delta$ sinogram. (b) $R^* \frac{\mathrm{d}^2}{\mathrm{d}E^2} R\delta$. (c) Landweber.

(d) $R\chi_B$ sinogram. (e) $R^* \frac{\mathrm{d}^2}{\mathrm{d}E^2} R\chi_B$. (f) Landweber.

Figure 3. *Broken-ray transform reconstructions of the delta function at* $(0,1)$. *Two edges of the data set are highlighted in each case, which correspond to artifacts in the reconstruction. These are highlighted in the Landweber image.*

We see vertical and horizontal blurring due to limited data in the Landweber iteration. This is because not all wavefront directions are visible with broken-ray data, as described by Theorem 3.12. This effect is illustrated in Figure 2a. We can see that there is only limited angular coverage on the boundary of B and at $(0,1)$ (the location of δ), where the test phantoms have singularities. Additionally, we see artifacts appearing along broken-rays at the boundary of the data set. This is due to the sharp cutoff in the sinogram space (see Figures 3a and 3d). We see similar boundary artifacts occurring in [3] in reconstructions from limited line integral data. Two boundary points in the support of $\chi_A Rf$ are labelled by "Edge 1" and "Edge 2" in the sinograms of Figures 3a and 3d, and they generate artifacts that are shown along broken-ray curves in the image reconstructions of Figures 3c and 3f. The broken-ray curves in the image space are labelled similarly by "Edge 1" and "Edge 2," as in sinogram space. Note that only half of the broken-ray curve at Edge 2 intersects $[-1,1]\times[0,2]$, and hence the Edge 2 artifacts appear along lines in Figures 3c and 3f. Similar boundary artifacts are observed in [5], where the authors present reconstructions of χ_B and a Shepp–Logan phantom from Rf. The upper E limit used by [5] (E is equivalent to the cone opening angle ω, in the notation of [5]) is greater than the maximum E used here, however, and hence the reconstructions [5] better resolve the horizontal singularities.

If artifacts due to a Λ (as in Remark 3.5) are present, we would expect to see them highlighted in the FBP reconstruction (as in [40]). This is not the case, however, and there is no evidence of Λ artifacts. This is as predicted by our theory and is in line with the results of [35, Theorem 14] for a related but overdetermined transform which show that the normal operator R^*R is a PDO when $q = q_C$.

Example 4.2 (BST: Bolker satisfied). The curves of integration in BST are [41]

$$q_B(r) = \frac{r}{\sqrt{r^2+1}}.$$

See Figure 1 for an example of the Bragg curve when $x_0 = 3$ and $E = 2$. q_B describes the integration curves for the central scanning profile $x_2 = 0$, using the notation of [41]. Explicitly we set $x_2 = 0$ in [41, eq. (4.2)] to obtain q_B. For an analysis of the general case when $x_2 \in (-1,1)$, see Appendix B.

The first and second order derivatives of q_B are

$$q_B'(r) = \frac{1}{(r^2+1)^{\frac{3}{2}}} \neq 0, \quad q_B''(r) = -\frac{3r}{(r^2+1)^{\frac{5}{2}}}.$$

Hence $g_B(r) = \frac{q'(r)}{q(r)} = \frac{1}{r(r^2+1)}$, which is injective on $(0,\infty)$, and it follows that

$$g_B'(r) = \frac{q''(r)}{q(r)} - \frac{q'(r)^2}{q^2(r)} = -\frac{3r^2+1}{r^2(r^2+1)^2} < 0.$$

Thus the semiglobal Bolker assumption holds for R when $q = q_B$ in BST. See Figure 4 for reconstructions of $f = \delta$ and $f = \chi_B$ from Rf, when $q = q_B$. The scanning region is $[-1,1]\times[0,2]$, and Rf is simulated for $E \in (0, 2.83)$ and $x_0 \in [-2,2]$, as in Example 4.1. We see artifacts appearing along Bragg curves at the boundary of the data set, due to the

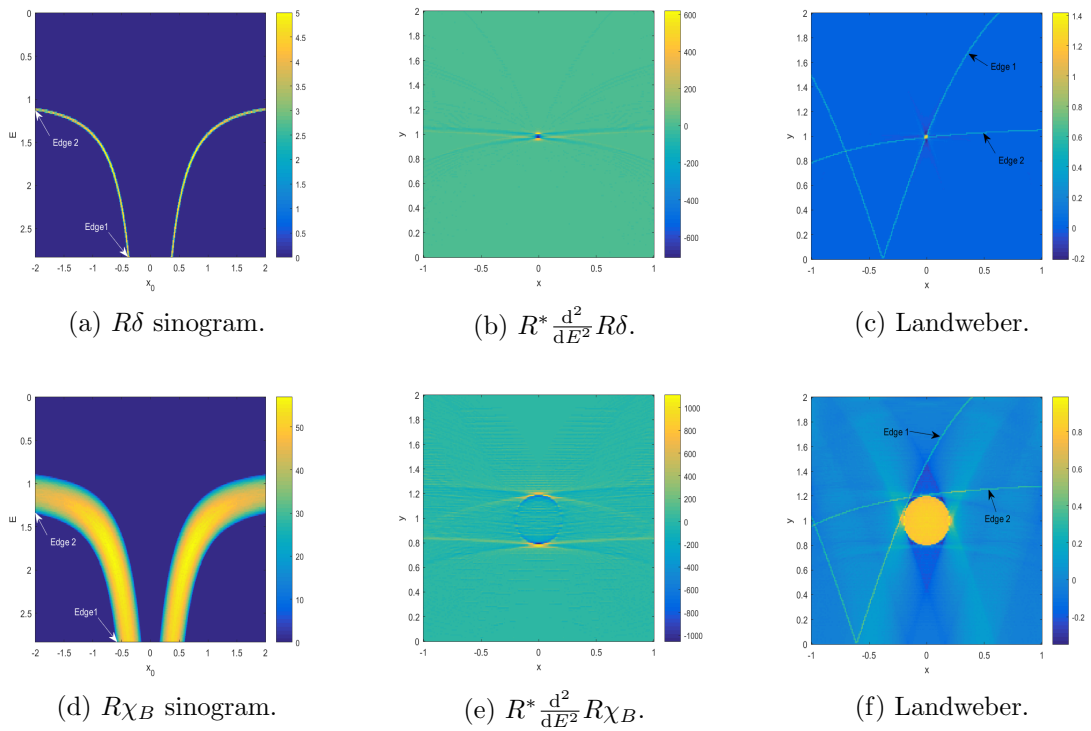

(a) $R\delta$ sinogram. (b) $R^* \frac{\mathrm{d}^2}{\mathrm{d}E^2} R\delta$. (c) Landweber.

(d) $R\chi_B$ sinogram. (e) $R^* \frac{\mathrm{d}^2}{\mathrm{d}E^2} R\chi_B$. (f) Landweber.

Figure 4. *Bragg transform reconstructions. Two edges of the data set are highlighted in each case, which correspond to artifacts in the reconstruction. These are highlighted in the Landweber image.*

cutoff in sinogram space. The points on the sinograms in Figures 4a and 4d labeled "Edge 1" and "Edge 2" are in the support of the data and on the boundary of the data set; the sharp cutoff at the boundary creates artifacts as highlighted along Bragg curves (which are labeled "Edge 1" and "Edge 2" in Figures 4c and 4f). Similar to Example 4.1, only half of the Bragg curve at Edge 2 intersects $[-1,1] \times [0,2]$, and hence the Edge 2 artifacts appear along one-sided Bragg curves (minus the reflected curve in $x = x_0$) in Figures 3c and 3f. There is a horizontal and vertical blurring due to limited data in the Landweber reconstruction. This observation is in line with the theory of section 3.4 and Theorem 3.12. We noticed a similar effect in reconstructions from broken-ray curves, when $q = q_C$ in Example 4.1. In this case the vertical blurring is less pronounced. The vertical singularities appear sharper in the FBP reconstructions also. This is because of the flatter gradients of the Bragg curves as $r \to \infty$, compared to straight lines, which allow the Bragg curves to better detect vertical singularities. That is, the Bragg curves are such that

$$0 = \lim_{r\to\infty} q_B'(r) < \min\left(\{q_C'(r) : r \in [0,\infty)\}\right) = 1.$$

See Figure 5 for a visualization. We display a shifted Bragg curve q_B and Compton curve q_C. q_B and q_C intersect on the boundary of χ_B at $(0, 1.2)$, where a singularity occurs in the direction $(0,1)$ (a vertical singularity). The gradients at $(0, 1.2)$ are $q_C'(0) = 1.2$ and $q_B'(0) \approx 0.6$, approximately half the gradient of q_C at $(0, 1.2)$. The reduction in gradient

allows for better detection of the singularity at $(0, 1.2)$ using Bragg curves.

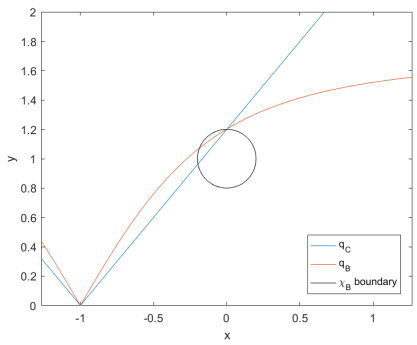

Figure 5. *Illustration of Compton versus Bragg, vertical edge detection.*

Example 4.3 (sinusoidal curves: Bolker not satisfied). Here we give an example q which satisfies (3.1), but fails to satisfy the semiglobal Bolker assumption. We define the sinusoidal curves as

$$q_S(r) = (1+\epsilon)r + \sin r, \tag{4.2}$$

where $\epsilon > 0$. See Figure 6a. We can check that $q_S(0) = 0$ and $q_S'(r) = (1+\epsilon) + \cos r > \epsilon > 0$, and hence (3.1) is satisfied. As (3.1) holds, it follows that R is injective by [41, Theorem 5.2], and hence there are no artifacts due to null space. At this stage, we are not aware of a practical application where the sinusoidal curves apply. We consider this example purely to verify our microlocal theory in the case where the conditions of Theorem 3.1 are not satisfied, and to show that the artifacts are exactly as predicted by the theory. This is important to show how such artifacts can appear when using a variety of reconstruction methods, and that we can predict their locations exactly.

We have

$$g_S(r) = \frac{(1+\epsilon) + \cos r}{(1+\epsilon)r + \sin r},$$

which is noninjective. See Figure 6b. Further, $g_S'(r) = \frac{g_1(r)}{q_S^2(r)}$, where

$$g_1(r) = (1+\epsilon)\big(r\sin r + 2\cos r\big) + (1+\epsilon)^2 + 1,$$

and hence $g_S'(r) = 0 \iff g_1(r) = 0$, for $r \in (0, \infty)$. g_1 is zero for infinitely many $r \in \mathbb{R}$, for any ϵ chosen. See Figure 6c. Hence for the sinusoidal curves the semiglobal Bolker assumption is not satisfied, and we can expect to see artifacts due to Λ (see Remark 3.5) in the reconstruction. We note that R is injective by [41, Theorem 5.2] and hence we expect no additional artifacts due to null space. The scanning region used in this example is $[-10, 10] \times [0, 20]$, and Rf is simulated for $E \in (0, 3.77)$ and $x_0 \in [-20, 20]$. We scale up by a factor of 10 in this case to allow for multiple oscillations of the sinusoidal curves within the scanning region. See Figure 6a. On $[-1, 1] \times [0, 2]$ (the scanning region used in Examples 4.1 and 4.2), the q_S curves are appear approximately as broken-rays (V-lines) in the simulations, since

$\sin r \approx r$ for r close to zero. Hence we scale the scanning region size by 10 here to better highlight the discrepancies between broken-ray and sinusoidal transform reconstruction. In these dimensions the x_0 range used is the same (relatively speaking) as in Examples 4.1 and 4.2. The energy range is chosen so that the integration curves have a wide variety of gradients, and sufficiently cover $[-10, 10] \times [0, 20]$.

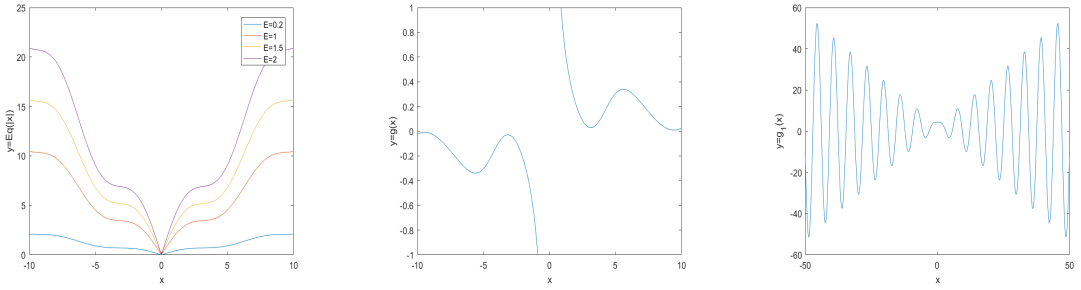

(a) Eq_S for $E \in \{0.2, 1, 1.5, 2\}$. (b) g_S. (c) g_1.

Figure 6. *The curves q_S, g_S, and g_1 for $\epsilon = 0.1$. Note that the x and y axis limits vary across subfigures* (a), (b), *and* (c).

See Figure 7 for reconstructions of $f = \delta$, centered at $(0, 10)$, from Rf, when $q = q_S$. As predicted, we see artifacts appearing in the reconstructions on the sinusoidal curves which intersect f normal to a singularity (equivalently, any curve which intersects $f = \delta$). As described in Remark 3.5, we use g_S to map the singularities of δ (at $(0, 10)$, in all directions) to artifacts along sinusoidal curves. The artifacts predicted by g_S and our theory are shown in Figure 7c. The same artifacts are observed in the FBP reconstruction in Figure 7d, and align exactly with our predictions. Note that we have removed the reconstructed delta function from Figure 7d (i.e., we set the central three image columns to zero) and truncated the color bars to better show the artifacts. The artifacts are also observed faintly in the Landweber reconstruction in Figure 7b. This is in line with the theory of [40], where the microlocal artifacts are shown to be highlighted in FBP reconstructions.

Let $B = \{(x, y) \in \mathbb{R}^2 : x^2 + (y - 10)^2 < 4\}$. See Figure 8 for reconstructions of $f = \chi_B$ from Rf. Similar to the $f = \delta$ case, we see artifacts appearing on the sinusoidal curves which are tangent to the boundary of χ_B (i.e., the set of points where f has singularities). See Figure 8b. Further, q_S has a larger range of gradients, when compared to q_C and q_B. That is, $\mu\big(q_S'([0,\infty))\big) > \mu\big(q_C'([0,\infty))\big), \mu\big(q_B'([0,\infty))\big)$, where μ is a Lebesgue measure. Hence the generalized Radon data can resolve the image singularities in more directions with sinusoidal curves, when compared to BST and CST curves. See Figure 5 and the arguments towards the end of Example 4.2. Due to the increased range of gradients, the horizontal and vertical blurring effects observed in Examples 4.1 and 4.2 are less prominent here. This is evidenced by Figure 8c.

5. Conclusions and further work. Here we have presented a novel microlocal analysis of a generalized cone Radon transform R, which defines the integrals of $f \in L^2_c(\mathbb{R}^{n-1} \times (0, \infty))$ over the $(n-1)$-dimensional surfaces of revolution of smooth curves q. We proved that R is an elliptic FIO of order $\frac{1-n}{2}$, and we gave an explicit expression for the left projection Π_L.

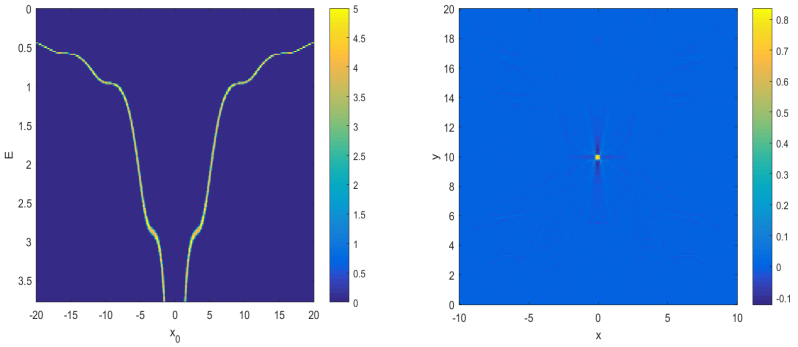

(a) $R\delta$ sinogram. (b) Landweber.

(c) Λ artifacts. (d) $R^* \frac{\mathrm{d}^2}{\mathrm{d}E^2} R\delta$.

Figure 7. *Sinusoid transform reconstructions of $f = \delta$.*

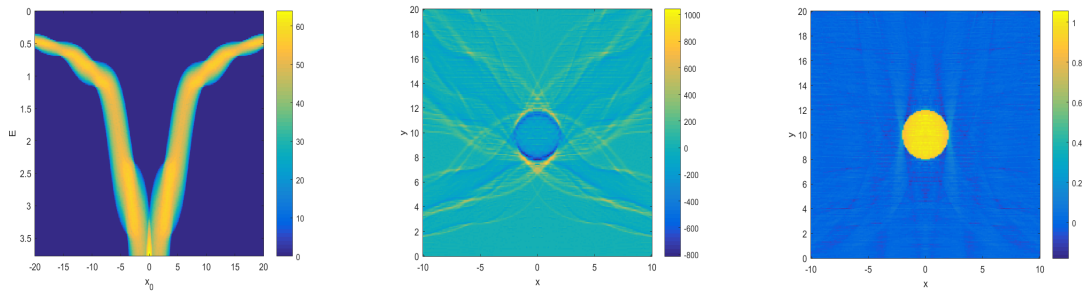

(a) $R\chi_B$ sinogram. (b) $R^* \frac{\mathrm{d}^2}{\mathrm{d}E^2} R\chi_B$. (c) Landweber.

Figure 8. *Sinusoid transform reconstructions of $f = \chi_B$.*

Our main theorem (Theorem 3.1) shows that Π_L satisfies the semiglobal Bolker assumption if and only if $g = q'/q$ is an immersion. When $n = 2$, in the case when the conditions of Theorem 3.1 are not satisfied, the matrix $D\Pi_L$ (of (3.13)) drops rank by 1, and hence the projections Π_L and Π_R exhibit singularities (e.g., of fold or blowdown type) of order 1 on $\{g' = 0\}$. In Remark 3.5 we provided implicit expressions for the image artifacts associated

with the $\{g' = 0\}$ singularities in two dimensions. In further work we aim to analyze how the type of singularity (e.g., fold or blowdown) varies with q and the dimension n. In section 3.4 we provided Sobolev smoothing estimates for the generalized Radon transforms and gave an analysis of the visible singularities when $n = 2$. In future work we aim to determine the visible singularities in generalized Radon data when $n \geq 3$, particularly in the $n = 3$ case as this is of practical interest.

Two main applications of our theory are in Compton camera imaging in ECST, and crystalline structure imaging in BST and airport baggage screening. In section 4 we showed that the ECST and BST integration curves satisfied the conditions of Theorem 3.1, thus proving that the ECST and BST generalized Radon FIO satisfy the semiglobal Bolker assumption. Additionally, we gave example "sinusoidal" q in Example 4.3 for which the corresponding generalized Radon transforms violate the semiglobal Bolker assumption, and we provided simulated image reconstructions from sinusoidal Radon data. We saw artifacts appearing along the sinusoidal curves which intersected the singularities of f normal to the direction of the singularity. The artifacts observed in reconstruction were shown to align exactly with our predictions in Remark 3.5 and the results of Theorem 3.1.

The theory presented here explains some key microlocal properties of a range of generalized Radon transformations in $\mathbb{R}^n$, whereby the integrals are taken over generalized cones with vertex constrained to the $\mathbf{x}' = (x_1, \ldots, x_{n-1})$ plane. In further work we aim to generalize the set of cone vertices to suit a wider range of imaging geometries. For example, we could consider the vertex sets which are smooth $n-1$ manifolds in $\mathbb{R}^n$, in a similar vein to [42] in $\mathbb{R}^3$.

It is noted that quality of reconstruction (with zero noise), from ECST and BST data, is low using the methods considered, and there are significant boundary artifacts in the reconstructions presented (see Examples 4.1 and 4.2). The reconstruction methods used here were chosen to highlight the image artifacts predicted by our theory, so this is as expected. In future work we aim to conduct a simulation study with noisy data, and derive practical reconstruction algorithms and regularization penalties to combat the artifacts, for example, using smoothing filters as in [5, 13, 3] to remove boundary artifacts. An algebraic approach may also prove fruitful (as is discovered in [39] for ECST artifacts), as this would allow us to apply the powerful regularization methods from the discrete inverse problems literature, e.g., total variation. In the reconstructions presented in Figures 3 and 4 we saw boundary artifacts corresponding to edges of the sinogram on the E and x_0 boundary, denoted "Edge 1" and "Edge 2," respectively. We noticed that the Edge 2 artifacts appeared more strongly in the FBP reconstructions, whereas in the Landweber reconstruction the artifacts appeared to have equal strength. In future work we aim to determine why the Edge 2 artifacts are stronger in the FBP reconstruction, e.g., this could be due to a numerical error.

Appendix A. Proof of Lemma 3.3.

In this appendix we provide proof of Lemma 3.3. We first restate the lemma and give proof thereafter.

Lemma 3.3. *There is a smooth function $\widetilde{\Psi} : Y \times X \to \mathbb{R}$ that is equal to Ψ on an open neighborhood V of*

$$\mathcal{S} = \{(E, \mathbf{x}_0, \mathbf{x}) \in Y \times X : \mathbf{x} \in S(E, \mathbf{x}_0)\}.$$

For $(E, \mathbf{x}_0, \mathbf{x}) \in Y \times X$, $\widetilde{\Psi}(E, \mathbf{x}_0, \mathbf{x}) = 0$ if and only if $\Psi(E, \mathbf{x}_0, \mathbf{x}) = 0$.

Proof. Note that $q : [0,\infty) \to [0,\infty)$ is continuous and $\forall r \in (0,\infty)$, $q'(r) \neq 0$. Therefore, $q^{-1} : q([0,\infty)) \to [0,\infty)$ is continuous with $q^{-1}(0) = 0$. Furthermore, by the inverse function theorem, $q^{-1} : q\big((0,\infty)\big) \to (0,\infty)$ is smooth (and strictly increasing).

Define

$$\mathcal{O} = \left\{(E, \mathbf{x}_0, \mathbf{x}) \in Y \times X : \mathbf{x}_0 = \mathbf{x}'\right\}. \tag{A.1}$$

Then, $\mathcal{O}$ is the set on which Ψ is not smooth.

For $(E, \mathbf{x}_0, \mathbf{x}) \in Y \times X$, let

$$H(E, \mathbf{x}_0, \mathbf{x}) = \frac{\left\|\mathbf{x}' - \mathbf{x}_0\right\|}{q^{-1}\big(x_n/E\big)}. \tag{A.2}$$

Then, H is continuous on $Y \times X$ and smooth except on $\mathcal{O}$. Let

$$U := H^{-1}\big((-1/4, 1/4)\big), \qquad V = H^{-1}\big((1/2,\infty)\big). \tag{A.3}$$

Because H is continuous, U is an open neighborhood of $\mathcal{O} = H^{-1}\big(\{0\}\big)$ and V is an open neighborhood of $\mathcal{S} = H^{-1}\big(\{1\}\big)$.

Let $\varphi : \mathbb{R} \to [0,1]$ be an even, smooth cutoff function that is equal to 0 on $(-1/4, 1/4)$ and equal to 1 on $(1/2,\infty)$. Therefore, $\varphi(H(E, \mathbf{x}_0, \mathbf{x}))$ is equal to 0 on the neighborhood U of $\mathcal{O}$ and equal 1 on the neighborhood V of $\mathcal{S}$.

Now, define

$$\widetilde{\Psi}(E, \mathbf{x}_0, \mathbf{x}) = \big(x_n - Eq(\left\|\mathbf{x}' - \mathbf{x}_0\right\|)\, \varphi\big(H(E, \mathbf{x}_0, \mathbf{x})\big)\big). \tag{A.4}$$

By the definition of H, $\widetilde{\Psi}(E, \mathbf{x}_0, \mathbf{x})$ is smooth because $\varphi(H(E, \mathbf{x}_0, \mathbf{x}))$ is zero in the neighborhood U of $\mathcal{O}$, the set on which Ψ is nondifferentiable. Furthermore, $\widetilde{\Psi}(E, \mathbf{x}_0, \mathbf{x}) = \Psi(E, \mathbf{x}_0, \mathbf{x})$ in the neighborhood V of $\mathcal{S}$ because $\varphi = 1$ on $(1/2,\infty)$.

Finally, we explain why $\widetilde{\Psi} = 0$ only on $\mathcal{S}$. For points inside $\mathcal{S}$ (i.e., points in the component of $\big(Y \times X\big) \setminus \mathcal{S}$ containing $\mathcal{O}$), $x_n > Eq(\left\|\mathbf{x}' - \mathbf{x}_0\right\|)$ because q is strictly increasing. In addition, since $\varphi \leq 1$, $x_n > Eq(\left\|\mathbf{x}' - \mathbf{x}_0\right\|)\, \varphi(H(E, \mathbf{x}_0, \mathbf{x}))$ and $\widetilde{\Psi}$ is never 0 inside $\mathcal{S}$. Note that $\Psi = 0$ only on $\mathcal{S}$. As $\widetilde{\Psi} = \Psi$ for points on $\mathcal{S}$ and points outside $\mathcal{S}$ ($\varphi = 1$ there), $\widetilde{\Psi} = 0$ on $\mathcal{S}$ and at no other point. This finishes the proof. ∎

Appendix B. Bragg curve analysis for $x_2 \in (-1, 1)$. Throughout this section we will use the notation of [41], where $x_2 \in (-1, 1)$ now describes the coordinates of the scanned line profile in BST (i.e., the vertex of the V is at the point (x_1, x_2) (see [41, Figure 1])); $x_1 \in \mathbb{R}$ plays the same role in both articles.

In [41] the authors consider a 1-D set of 2-D Radon transforms, with imaging applications in BST and spectroscopy. In Example 4.2 we considered the curves of integration defined by $q_B(x_1) = \frac{x_1}{\sqrt{x_1^2+1}}$. These curves describe a special case of the Radon transforms of [41], where the scanned line profile is on the centerline of the imaging apparatus, $x_2 = 0$. Here we consider the general $x_2 \in (-1, 1)$ case. The full set of integration curves in BST are described by [41, eq. (4.2)]

$$q_B(x_1, x_2) = \frac{1}{\sqrt{2}} \sqrt{1 + \frac{x_1^2 - (1 - x_2^2)}{\sqrt{x_1^2 + (x_2 + 1)^2}\sqrt{x_1^2 + (1 - x_2)^2}}}. \tag{B.1}$$

Note that $q_B(x_1, 0) = \frac{x_1}{\sqrt{x_1^2+1}}$. In [41] the 1-D set of Radon transforms considered take integrals over the broken-ray curves $q_B(\cdot, x_2)$ for each $x_2 \in (-1, 1)$. The broken-ray integrals are described by the generalized cone transform of (3.4) for $\mathbb{R}^2$ with $q = q_B(\cdot, x_2)$. Note that $q_B(\cdot, x_2) > 0$ for $x_1 > 0$, for every $x_2 \in (-1, 1)$, so (3.1) is satisfied. Here we aim to show that $h_B(\cdot, x_2) = \frac{1}{g_B(\cdot, x_2)} = \frac{q_B(\cdot, x_2)}{q_B'(\cdot, x_2)}$ is an immersion for each $x_2 \in (-1, 1)$, thus showing that the semiglobal Bolker assumption is satisfied for every scanning profile considered. As the calculation of the second order derivatives of q_B in x_1 is cumbersome, we verify Bolker numerically for some chosen range of x_1, x_2. Note that we consider the reciprocal h_B of g_B here to avoid division by values close to zero as $x_1 \to 0$, and since $g_B'(\cdot, x_2) = 0 \iff h_B'(\cdot, x_2) = 0$ for $g_B(\cdot, x_2) : (0, \infty) \to (0, \infty)$. We choose to simulate h_B' for $x_1 \in (0, 3]$ and $x_2 \in (-1, 1)$. The maximum x_1 (i.e., $x_1 = 3$) chosen is the maximum x_1 considered in the scanning setup of Example 4.2. That is with scanning region $[-1, 1] \times [0, 2]$ and $x_0 \in [-2, 2]$ (the maximum x_1 occurs when $x_0 = -2, 2$ at the edge of the scanning region). We need only consider positive x_1 since q_B of (B.1) is symmetric in x_1 about $x_1 = 0$. See Figure 9, where we display h_B' on $(0, 3] \times (-1, 1)$. Finite differences are used to approximate the derivatives. The minimum value of h_B' in this range is $\min_{(0,3]\times(-1,1)}(h_B') \approx 1$, which indicates that the semiglobal Bolker assumption is satisfied in the scanning geometry of Example 4.2.

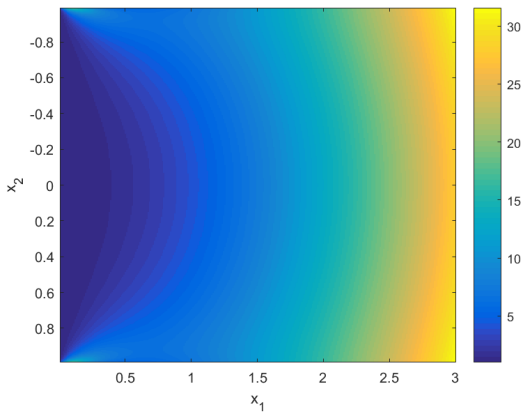

(a) $h_B'(x_1, x_2)$. $\min_{(0,3]\times(-1,1)}(h_B') \approx 1$.

Figure 9. *Numerical validation of $h_B'(\cdot, x_2) \neq 0$ for each $x_2 \in (-1, 1)$.*

Acknowledgments. First, it is our pleasure to thank the referees for their thoughtful, thorough reviews that improved this article. We would like to thank Professor Eric Miller for his helpful suggestions, thoughts, and insight towards this article, in particular towards improving the readability of this article and helping us communicate the main ideas to a practical audience. This material is based upon work supported by the U.S. Department of Homeland Security, Science and Technology Directorate, Office of University Programs, under grant 2013-ST-061-ED0001. The views and conclusions contained in this document are those of the authors and should not be interpreted as necessarily representing the official policies, either expressed or implied, of the U.S. Department of Homeland Security.

REFERENCES

[1] G. Ambartsoumian, *Inversion of the V-line Radon transform in a disc and its applications in imaging*, Comput. Math. Appl., 64 (2012), pp. 260–265.

[2] G. Ambartsoumian and M. J. Latifi Jebelli, *The V-line transform with some generalizations and cone differentiation*, Inverse Problems, 35 (2019), 034003, https://doi.org/10.1088/1361-6420/aafcf3.

[3] L. Borg, J. Frikel, J. S. Jørgensen, and E. T. Quinto, *Analyzing reconstruction artifacts from arbitrary incomplete X-ray CT data*, SIAM J. Imaging Sci., 11 (2018), pp. 2786–2814, https://doi.org/10.1137/18M1166833.

[4] J. Cebeiro, M. Morvidone, and M. Nguyen, *Back-projection inversion of a conical Radon transform*, Inverse Probl. Sci. Eng., 24 (2016), pp. 328–352.

[5] J. Cebeiro, M. A. Morvidone, and M. K. Nguyen, *The Radon transform on V-lines: Artifact analysis and image enhancement*, in Proceedings of the XVII Workshop on Information Processing and Control (RPIC), IEEE, 2017, pp. 1–6.

[6] A. M. Cormack, *Radon's problem for some surfaces in* $\mathbf{R}^n$, Proc. Amer. Math. Soc., 99 (1987), pp. 305–312, https://doi.org/10.2307/2046630.

[7] J. J. Duistermaat, *Fourier Integral Operators*, Progr. Math. 130, Birkhäuser, Boston, 1996.

[8] J. J. Duistermaat and L. Hörmander, *Fourier integral operators,* II, Acta Math., 128 (1972), pp. 183–269.

[9] R. Felea, R. Gaburro, and C. J. Nolan, *Microlocal analysis of SAR imaging of a dynamic reflectivity function*, SIAM J. Math. Anal., 45 (2013), pp. 2767–2789, https://doi.org/10.1137/120873571.

[10] L. Florescu, V. A. Markel, and J. C. Schotland, *Single-scattering optical tomography: Simultaneous reconstruction of scattering and absorption*, Phys. Rev. E, 81 (2010), 016602.

[11] L. Florescu, V. A. Markel, and J. C. Schotland, *Inversion formulas for the broken-ray Radon transform*, Inverse Problems, 27 (2011), 025002.

[12] L. Florescu, J. C. Schotland, and V. A. Markel, *Single-scattering optical tomography*, Phys. Rev. E, 79 (2009), 036607.

[13] J. Frikel and E. T. Quinto, *Artifacts in incomplete data tomography with applications to photoacoustic tomography and sonar*, SIAM J. Appl. Math., 75 (2015), pp. 703–725, https://doi.org/10.1137/140977709.

[14] R. Gouia-Zarrad and G. Ambartsoumian, *Exact inversion of the conical Radon transform with a fixed opening angle*, Inverse Problems, 30 (2014), 045007, https://doi.org/10.1088/0266-5611/30/4/045007.

[15] V. Guillemin and S. Sternberg, *Geometric Asymptotics*, American Mathematical Society, Providence, RI, 1977.

[16] M. Haltmeier, *Exact reconstruction formulas for a Radon transform over cones*, Inverse Problems, 30 (2014), 035001.

[17] L. Hörmander, *Fourier integral operators,* I, Acta Math., 127 (1971), pp. 79–183.

[18] L. Hörmander, *The Analysis of Linear Partial Differential Operators* I*: Distribution Theory and Fourier Analysis*, Classics Math., reprint of the second (1990) edition, Springer-Verlag, Berlin, 2003.

[19] L. Hörmander, *The Analysis of Linear Partial Differential Operators* III*: Pseudo-Differential Operators*, reprint of the 1994 edition, Classics Math., Springer, Berlin, 2007, https://doi.org/10.1007/978-3-540-49938-1.

[20] L. Hörmander, *The Analysis of Linear Partial Differential Operators* IV*: Fourier Integral Operators*, Classics Math., reprint of the 1994 edition, Springer-Verlag, Berlin, 2009, https://doi.org/10.1007/978-3-642-00136-9.

[21] C.-Y. Jung and S. Moon, *Inversion formulas for cone transforms arising in application of Compton cameras*, Inverse Problems, 31 (2015), 015006.

[22] P. Kuchment and F. Terzioglu, *Three-dimensional image reconstruction from Compton camera data*, SIAM J. Imaging Sci., 9 (2016), pp. 1708–1725, https://doi.org/10.1137/16M107476X.

[23] Á. Kurusa, *Support curves of invertible Radon transforms*, Arch. Math. (Basel), 61 (1993), pp. 448–458, https://doi.org/10.1007/BF01207544.

[24] V. Maxim, M. Frandeş, and R. Prost, *Analytical inversion of the Compton transform using the full set of available projections*, Inverse Problems, 25 (2009), 095001.

[25] S. Moon, *On the determination of a function from its conical Radon transform with a fixed central axis*,

SIAM J. Math. Anal., 48 (2016), pp. 1833–1847, https://doi.org/10.1137/15M1021945.
[26] S. Moon, *Inversion of the conical Radon transform with vertices on a surface of revolution arising in an application of a Compton camera*, Inverse Problems, 33 (2017), 065002.
[27] S. Moon and M. Haltmeier, *Analytic inversion of a conical radon transform arising in application of Compton cameras on the cylinder*, SIAM J. Imaging Sci., 10 (2017), pp. 535–557, https://doi.org/10.1137/16M1083116.
[28] M. Morvidone, M. K. Nguyen, T. T. Truong, and H. Zaidi, *On the V-line Radon transform and its imaging applications*, Int. J. Biomed. Imaging, 2010 (2010), 208179.
[29] M. K. Nguyen, T. T. Truong, and P. Grangeat, *Radon transforms on a class of cones with fixed axis direction*, J. Phys. A, 38 (2005), pp. 8003–8015.
[30] V. P. Palamodov, *A uniform reconstruction formula in integral geometry*, Inverse Problems, 28 (2012), 065014.
[31] B. E. Petersen, *Introduction to the Fourier Transform & Pseudodifferential Operators*, Monogr. Stud. Math. 19, Pitman, Boston, 1983.
[32] E. T. Quinto, *The dependence of the generalized Radon transform on defining measures*, Trans. Amer. Math. Soc., 257 (1980), pp. 331–346.
[33] E. T. Quinto, *Singularities of the X-ray transform and limited data tomography in* $\mathbb{R}^2$ *and* $\mathbb{R}^3$, SIAM J. Math. Anal., 24 (1993), pp. 1215–1225, https://doi.org/10.1137/0524069.
[34] W. Rudin, *Functional Analysis*, McGraw-Hill Series in Higher Mathematics, McGraw-Hill, New York, 1973.
[35] F. Terzioglu, *Some analytic properties of the cone transform*, Inverse Problems, 35 (2019), 034002.
[36] F. Terzioglu, P. Kuchment, and L. Kunyansky, *Compton camera imaging and the cone transform: A brief overview*, Inverse Problems, 34 (2018), 054002, https://doi.org/10.1088/1361-6420/aab0ab.
[37] T. T. Truong and M. K. Nguyen, *New properties of the V-line Radon transform and their imaging applications*, J. Phys. A: Math. Theor., 48 (2015), 405204.
[38] T. T. Truong, M. K. Nguyen, and H. Zaidi, *The mathematical foundations of 3D Compton scatter emission imaging*, Int. J. Biomed. Imaging, 2007 (2007), 092780.
[39] J. Webber and E. T. Quinto, *Microlocal analysis of a Compton tomography problem*, SIAM J. Imaging Sci., 13 (2020), pp. 746–774, https://doi.org/10.1137/19M1251035.
[40] J. Webber, E. T. Quinto, and E. L. Miller, *A joint reconstruction and lambda tomography regularization technique for energy-resolved X-ray imaging*, Inverse Problems, 36 (2020), 074002.
[41] J. W. Webber and E. L. Miller, *Bragg Scattering Tomography*, preprint, https://arxiv.org/abs/2004.10961, 2020.
[42] Y. Zhang, *Recovery of singularities for the weighted cone transform appearing in Compton camera imaging*, Inverse Problems, 36 (2020), 025014.